

**Characterizing hydraulic parameters in a  
small-scale tank experiment, using  
Self-Potential, DC Resistivity and Induced  
Polarization methods.**

**Kristian Marnette**

Utrecht University, 2011

Supervised by:  
Dr. A. Revil<sup>1</sup> & Prof. Dr. R.J. Schotting<sup>2</sup>

August 29, 2011

<sup>1</sup>Colorado School of Mines, Golden, Colorado, USA

<sup>2</sup>Utrecht University, Utrecht, The Netherlands

# Contents

<b>Abstract</b>	<b>2</b>
<b>1 Introduction</b>	<b>4</b>
1.1 Geophysical methods for hydraulic parameter characterization . . . . .	4
1.2 Objectives . . . . .	6
<b>2 Theory</b>	<b>7</b>
2.1 Linear transport laws . . . . .	7
2.2 Darcy's law . . . . .	8
2.3 Self-potential (SP) . . . . .	8
2.3.1 Electric double layer model . . . . .	9
2.3.2 Streaming potential . . . . .	10
2.3.3 Saturated flow . . . . .	10
2.3.4 Unsaturated flow . . . . .	12
2.4 Direct Current Resistivity . . . . .	12
2.5 Induced Polarization (IP) . . . . .	14
<b>3 Experimental setup</b>	<b>16</b>
3.1 Equipment & setup . . . . .	16
<b>4 Transient experiment: Self-Potential (SP)</b>	<b>21</b>
4.1 Introduction . . . . .	21
4.2 Methods . . . . .	21
4.2.1 Pump . . . . .	22
4.2.2 Electrodes . . . . .	23
4.2.3 Acquisition system . . . . .	24
4.2.4 Electric coupling and reference electrode . . . . .	24
4.3 Resulting data & data processing . . . . .	25
4.3.1 Raw data . . . . .	25
4.3.2 Removing gain, resampling and reducing the data . . . . .	25
4.3.3 Polynomial curve fitting and detrending . . . . .	26
4.4 Forward modeling . . . . .	30
4.4.1 Initial values model . . . . .	30
4.4.2 Transient model . . . . .	32
4.4.3 Model improvement & data comparison . . . . .	35
4.5 Conclusions . . . . .	41

<b>5 Stationary experiment: Direct Current Resistivity (DC Resistivity) &amp; Induced Polarization (IP)</b>	<b>42</b>
5.1 Introduction . . . . .	42
5.2 Methods . . . . .	42
5.2.1 Electrodes and their placement . . . . .	42
5.2.2 ABEM and protocol . . . . .	44
5.2.3 Consequences of differing electrode spacing and array lengths . . . . .	47
5.3 Data . . . . .	49
5.3.1 RES3DINV . . . . .	49
5.4 Conclusions . . . . .	51
<b>6 Conclusions</b>	<b>52</b>
<b>A Example values for several parameters</b>	<b>53</b>
<b>B Modeling parameters</b>	<b>56</b>
<b>C ABEM 3D protocol and address file</b>	<b>59</b>
C.1 Protocol file . . . . .	59
C.2 Address file . . . . .	61
<b>Bibliography</b>	<b>63</b>
<b>List of figures</b>	<b>67</b>
<b>List of tables</b>	<b>71</b>

# Abstract

As part of a larger project that is concerned with the characterization of hydraulic parameters from electrical surface measurements, this thesis covers self-potential, DC resistivity and induced polarization measurements taken on a medium-scale setup. This writing aims to research whether it is possible to obtain hydraulic parameters (such as permeability) from transient SP experiments and from DC resistivity and IP measurements taken on a steady-state setup. This setup was constructed inside a fish tank and consisted of a bulk material of medium sand. Two sand columns were placed inside the medium sand and were of a finer and respectively coarser material than the bulk material. The transient recovery experiment has shown that the self-potential method is able to show subsurface heterogeneities. The subsurface sand columns in the experiment are even outlined by the raw SP data. A forward model for the transient SP recovery experiment was successfully built. The Pearson linear correlation coefficients between the modeled and measured data for the full 800s timespan, all lie within the 0.95 to 1.00 range and have an average of +/- 0.99. The model can now be used in future inversion efforts. The DC resistance data have been corrected for four insulating boundaries. The two short-side boundaries, however, have a water reservoir. Those might have influenced the DC resistivity data. An improvement can be made in those data. The resistivity has values between 30 and 60  $\Omega m$ . The IP data roughly shows the outlines of the coarse grained column and somewhat the finer grained column in the inverted data. Following this work, the SP data should be inverted. Using inversion codes for a combination of the SP and the DC resistivity and IP data sets should enable us to obtain higher quality information about permeability distributions in the aquifer.

---

# 1

## Introduction

### 1.1 Geophysical methods for hydraulic parameter characterization

The monitoring of the flow of fluids in the pore space of porous material is an important research topic for the monitoring of oil and gas reservoirs, in civil engineering, and in environmental geosciences. In traditional regional hydrological studies, wells are used to characterize the subsurface hydrological parameters. These wells are invasive and expensive, the data sampling locations arbitrarily chosen and the resulting data is precise, but discretely distributed. Discretely distributed, since wells give very local information of the parameters. Due to the inhomogeneous nature of the subsurface, well logging is inherently not the most representable and reliable technique for site-scale subsurface parameter characterization [Slater, 2007; Barlebo et al., 2004]. Geophysical methods give spatialized data, but are more uncertain.

Electrical and electromagnetic methods in geophysics form a set of powerful methods to perform in a minimally intrusive way such monitoring. In recent years, the interest in using electrical and electromagnetic methods to recover values for subsurface hydraulic parameters has increased. Since the beginning of this century, with increasing hydrocarbon prices and decreasing reserves, even the hydrocarbon exploration industry started to see the benefits of electromagnetic methods, such as the controlled-source electromagnetics method (CSEM) [Constable and Srnka, 2007].

DC resistivity tomography, for instance, has proven to be an affordable method to image the subsurface and to image dynamic processes such as salt water intrusion or change in temperature or water saturation for instance [Tsourlos and Ogilvy, 1999]. The self-potential (SP) method, initially used as a borehole technique that was patented by the Schlumberger brothers in the late 1930s [Schlumberger, 1939], can be used to estimate flow direction and flow velocity in the subsurface. (Spectral) Induced Polarization methods (SIP or IP) give us some information about the hydraulic parameters of the subsurface. None of these methods mentioned above are able to quantify all of the parameters of interest (architecture, hydraulic conductivity, porosity etc.) directly. Therefore more research has to be conducted to develop more knowledge on combining data from different geophysical methods [Slater, 2007]. Figure 1.1 provides a flowchart from Slater [2007], showing the present efforts to characterize aquifer geometries, using different types of geophysical data sets.

In geophysics, measurements are taken using sensors that are placed at discrete loca-

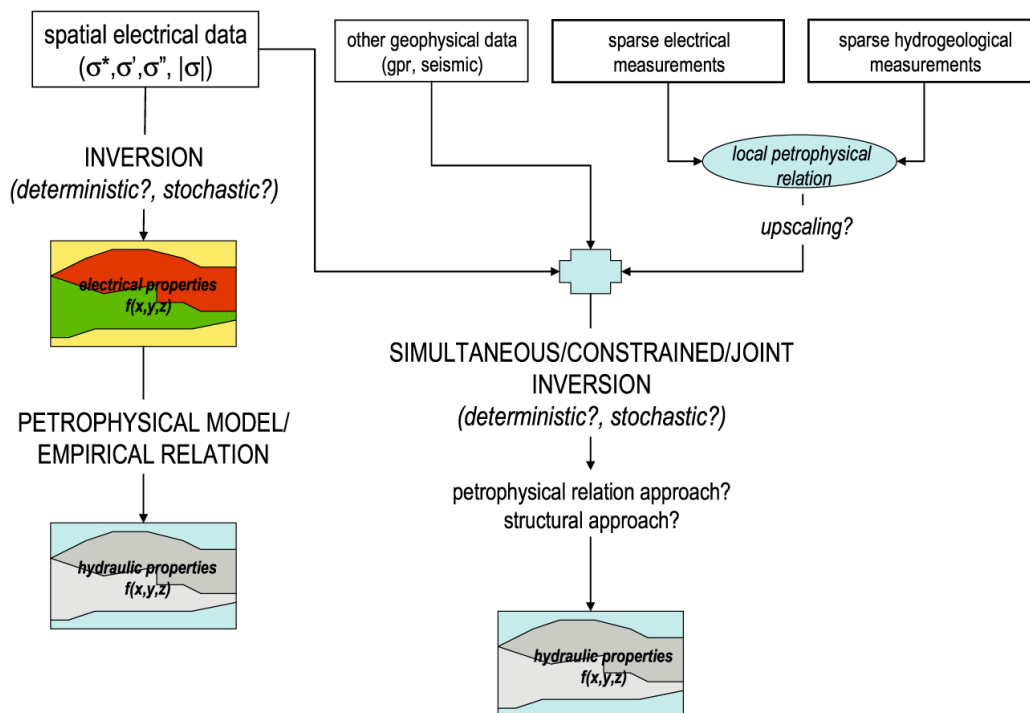


Figure 1.1: A flowchart, taken from Slater [2007], summarizing efforts to characterize aquifer geometries using geoelectrical measurements.

tions on or below the earth's surface in boreholes. Since measurements are conducted between (sets of) sensors, the data can be used to image between the location of the sensors (cross-borehole tomography) or the subsurface from surface measurements. This has a few advantages: 1) although distribution of sensors is still spatially discrete, the measured data represents a larger spatial spread and thus a better representation of the local/regional value for the sought parameter 2) inversion algorithms can be used to quantify an estimation of the parameters of interest at all locations within a 2D or 3D section of the studied area.

Retrieving the values for all locations is done by combining simultaneously (or within reasonable time in which the parameters are not changing dramatically) recorded data from several sensors or sets of sensors. The resulting data is essentially a section (tomogram) that indicates contrasts in the parameter of interest. Inversion algorithms of various data types have extensively been discussed in the literature (e.g. [Li and Oldenburg \[2000\]](#); [Loke et al. \[2006\]](#); [Minsley et al. \[2007a\]](#); [Jardani et al. \[2007\]](#)). Inversion algorithms are available for many different geophysical methods, including the methods used in this thesis. However, inversion techniques that combine data recorded with several different geophysical methods are currently in development. There are IP and SIP inversion codes that can take SP and DC resistivity inverted data as a priori information.

## 1.2 Objectives

This study is part of a project that aims at combining data of different geophysical methods to develop an integrated inversion technique to characterize the distribution of hydraulic parameters (like permeability) of an heterogeneous subsurface. In particular, this thesis is concerned with a transient self-potential experiment, modeling that SP experiment and describing the static DC-resistivity and IP measurements that were taken on an experimental setup.

In a recovery experiment, valuable information (for instance hydraulic conductivity) can be obtained [[Rushton, 2003](#)]. In this study it is tested if SP enables us to measure the subsurface flow in such a way that this information from the subsurface can be extracted. To retrieve more information about the grain properties in the aquifer, IP measurements were performed. In order to invert the apparent IP data, DC resistivity measurements were also needed.

A setup was needed that could handle a transient recovery experiment as well as a steady-state experiment. Furthermore, to increase the repeatability of the experiments and to be able to control experiment conditions, a scale model was built. This model consists of an aquifer in a fish tank that has an heterogeneous character. Two columns of different grain sizes were constructed to test for differing hydraulic parameters.

The transient recovery experiment will be modeled in Comsol. This forward model can be used in an iterative inversion process.

## 2

# Theory

### 2.1 Linear transport laws

According to Mitchell [1991], generally there are four different types of flow, each governed by its own set of constitutive and continuity equations (see Table 2.1). Whether there is a gradient in salinity in water, a gradient in electrical potential, or a gradient in water pressure, coupled flow mechanisms exist between the flux of ions, the current density, and the Darcy velocity (flux of water through a porous material).

Sensors have been developed that can measure the flow, or a different parameter that represents flow. The application of such sensors to transiently measure flow parameters, enables us to monitor flow behavior through time. Non-invasively measuring fluid flow using sensors is combined in the professional field of hydrogeophysics.

<b>FLOW <math>\Gamma</math></b>	<b>GRADIENT <math>\nabla \Phi</math></b>			
	Hydraulic potential	Temperature	Electrical potential	Chemical concentration
<i>Fluid</i>	<b>Darcy's Law</b> (hydraulic conduction)	Thermo-osmosis	Electro-osmosis	Chemical osmosis
<i>Heat</i>	Isothermal heat transfer	<b>Fourier's Law</b> (thermal conduction)	Peltier Effect	Dufour Effect
<i>Current</i>	Streaming current (streaming potential)	Seebeck Effect	<b>Ohm's Law</b> (electrical conduction)	Diffusion and membrane potentials
<i>Ionic (chemical)</i>	Streaming current	Soret Effect	Electrophoresis	<b>Fick's Law</b> (chemical diffusion)

Table 2.1: Primary and coupled flow phenomena (adapted from Mitchell [1991]).



## 2.2 Darcy's law

In the 19<sup>th</sup> century Henry Darcy developed a law for fluid flow through a porous medium [Darcy, 1856]. According to his law, fluid flow through a porous medium is dependent on the hydraulic head gradient and an intrinsic variable, the hydraulic conductivity.

The fluid flux  $Q$ , as defined by Darcy [1856], is

$$Q = \kappa \frac{\Delta h}{\Delta l} \quad (2.1)$$

where  $\Delta h$  is the difference in head over a horizontal distance  $\Delta l$ . If Equation 2.1 is now generalized for a homogenous and isotropic medium, the three-dimensional Darcy's velocity ( $\vec{u}$ ) equation is as follows

$$\vec{u} = -\kappa \vec{\nabla} h \quad (2.2)$$

The hydraulic head  $h$  is

$$h = z + \frac{p}{\rho_f g} \quad (2.3)$$

where  $z$  is an hydraulic head contribution due to the height of the water table with respect to an arbitrary reference elevation,  $p$  the contribution due to the local pressure,  $\rho_f$  the fluid's density and  $g$  the gravitational acceleration. The hydraulic conductivity ( $\kappa$ , from the German Konduktivität) is theoretically defined by:

$$\kappa = k \frac{\rho_f g}{\eta_f} \quad (2.4)$$

$k$  is permeability and  $\eta_f$  the dynamic viscosity of the fluid.

Combining Equation 2.2 with Equation 2.3 and Equation 2.4 and with the assumption that  $\rho_f$  and  $g$  are constant this will give

$$\vec{u} = -\frac{k}{\eta_f} \vec{\nabla} (p + \rho_f g z) \quad (2.5)$$

## 2.3 Self-potential (SP)

Self-potential signals result from an electrical potential that is measured between a fixed reference electrode and one or more electrodes in different locations, all on the surface, all in boreholes or a mixture of both. These potentials are natural and not induced by an active current injection. Although, self-potential values can reach up to 10 V [Castermant et al., 2008], the signals discussed in these experiments are minor (in the order of magnitude of mV). Measurements need to be taken with a high resolution (at least 0.1 mV), high input impedance (typically > 10 MOhm) DC-voltmeter.

In principle, there is four factors that contribute to this potential. Sorted in decreasing contribution:

hydraulic head gradient	→	streaming potential
redox potential gradient	→	electroredox effect
salinity gradient	→	diffusion potential
temperature gradient	→	thermoelectric effect

In the following we will be mainly interested in the streaming potential contribution associated with the flow of pore water.

The electroredox effect is a contribution to the self-potential signal caused by chemical reactions in the pore fluid or between the pore fluid and the grains. The redox potential can reach large numbers (in the order of hundreds of mV), when an electronic conductor is located in the subsurface. Two smaller contributions, that are in the present experiments small enough to be neglected, are the diffusion potential and the thermoelectric effect (the experiment was conducted at constant temperature). The former is caused by the diffusion of ions in a fluid, the latter by temperature gradients in the fluid.

Aside from signal sources there are also some noise sources, such as anthropogenic noise and lightning or telluric currents (ionosphere activity). Anthropogenic noise can be caused by nearby power lines, road traffic or noise sources that are inherent to the measurement equipment. The experiments as described in Chapter 3, were set up in order to decrease noise levels as much as possible.

### 2.3.1 Electric double layer model

The earliest model of a double layer was introduced by Hermann von Helmholtz in the 1850's [von Helmholtz, 1853]. The electrical double layer consists of the Stern and diffusive layers (Figure 2.1). The Stern layer [Stern, 1924] is composed of ions adsorbed directly onto the matrix surface by a host of chemical interactions. Screening this layer, the diffuse layer consists of ions loosely bounded to the matrix surface by Coulomb forces. This second layer is bounded much looser, because it is composed of free ions that move in the fluid under the influence of electric attraction and thermal motion, thus the name diffuse layer.

Revil and Florsch [2010] discuss that the Stern layer charge and the grain's surface charge are counterbalanced by the charges in the electrical diffuse layer. They define counterions as the ions with opposite charge of the fixed charge of the mineral surface and co-ions as charge carriers of same charge. The fixed mineral surface charge creates a Boltzmann distribution in the Coulombic field. The activity of the counterions and the co-ions obey this distribution (see Figure 2.1 (c)). A discrimination between the counterions in the Stern [Stern, 1924] and diffuse layers was introduced by Revil and Leroy [2004]. They define a partition coefficient of the counter charge,  $f$ . This coefficient is defined as

$$f = \frac{\sum_{i=1}^Q q_i \Gamma_i^S}{\sum_{i=1}^Q q_i \Gamma_i^S + \sum_{i=1}^Q q_i \Gamma_i^d} \quad (2.6)$$

where  $Q$  is the number of possible ionic species  $i$  that are present in the Stern layer and in the diffuse layer,  $q_i$  is the charge of species  $i$  (in  $C$ , positive or negative),  $\Gamma_i^S$  represents the surface site density of species  $i$  in the Stern layer (number of species  $i$  per unit surface area of the mineral water interface in  $m^2$ ), and  $\Gamma_i^d$  represents the equivalent surface site density of the diffuse layer (equivalent number of ion  $i$  of the diffuse layer per unit surface area of the mineral water interface, in  $m^2$ ). Aside from this partition coefficient, Revil and Florsch [2010] defined the total charge density of counterions per pore volume  $Q_v$  (in  $Cm^{-3}$ ). This variable contains the charge density of the pore water from the o-plane (see Figure 2.1(c)) and therefore includes the Stern layer.  $\bar{Q}_V$  is the charge density per unit of volume of solution in the medium due to the diffuse layer only. These two quantities are

related through the partition coefficient as follows

$$\bar{Q}_v = (1 - f)Q_v \quad (2.7)$$

and  $Q_v$  can be determined from the Cation Exchange Capacity of the rock

$$Q_v = \rho_s \frac{1 - \phi}{\phi} CEC \quad (2.8)$$

where  $\rho_s$  (in  $kgm^{-3}$ ) the mass density of the solid,  $\phi$  is the porosity and  $CEC$  is the cation exchange capacity (in  $Ckg^{-3}$ ), or the ability to exchange ions between the matrix and the pore fluid in a porous medium. The ions in the Stern layer can not be migrated by subsurface flow. Approxamately 85 to 98 % of the counterions are contained within the Stern layer, so  $\bar{Q}_v$ , is much smaller than  $Q_v$ . For example, some values of some of these parameters are reported in Appendix A.

### 2.3.2 Streaming potential

Following the classical Darcy's Law, an hydraulic head gradient in a saturated porous medium causes fluid flow. The existence of a streaming current (current flow associated with the advective drag of the charge density of the diffuse layer) along the flow of the pore water causes a source current density. In the continuity equation for the conservation of electrical charges (Equation 2.11), the divergence of the source current density is responsible for a source term in a Poisson equation for the electrical potential (Equation 2.13).

### 2.3.3 Saturated flow

The streaming potential response is in principal dependent on the following parameters: the cation exchange capacity (or CEC), the ionic mobilities and the electric conductivity of the subsurface. The CEC is the quantification of the activity of the grain's surface and is a proxy for how much free charge is present in the pore fluid. CEC has  $[mol/kg]$  units. The ionic mobility quantifies the mobility of ions and thus the mobility of charge through the fluid. Then the current density, induced by Darcy's flow, is shown by

$$\vec{J}_s = \bar{Q}_v \cdot \vec{u} \quad (2.9)$$

where  $\vec{J}_s$  is the current density,  $\bar{Q}_v$  is the excess of charge in the pore fluid and the diffusive layer (excluding therefore the Stern layer contribution) and  $\vec{u}$  is the Darcy's velocity. The total current density can then be written as

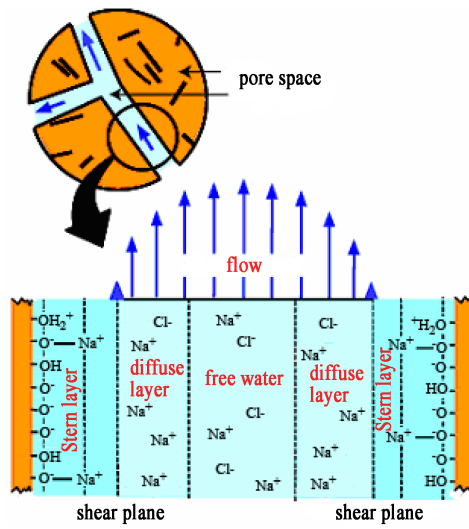
$$\vec{J} = -\sigma \vec{\nabla} \psi + \vec{J}_s \quad (2.10)$$

where  $\vec{J}$  is the total current density,  $\sigma$  the electrical conductivity (or the reciprocal of the electrical resistivity  $\rho$ ) of the porous material,  $\vec{\nabla} \psi$  the electrical field and  $\vec{J}_s$  the advective source term for the streaming potential. As an assumption, there is no input of current from a source outside the system. This means that Equation 2.10 must comply to

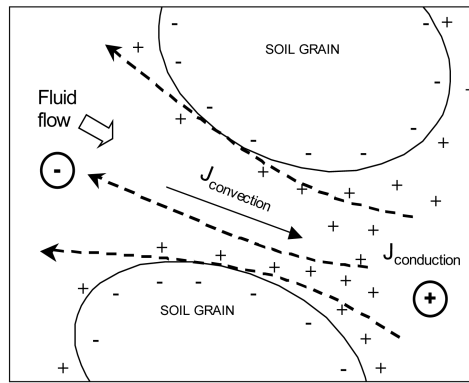
$$\vec{\nabla} \cdot \vec{J} = 0 \quad (2.11)$$

Giving us

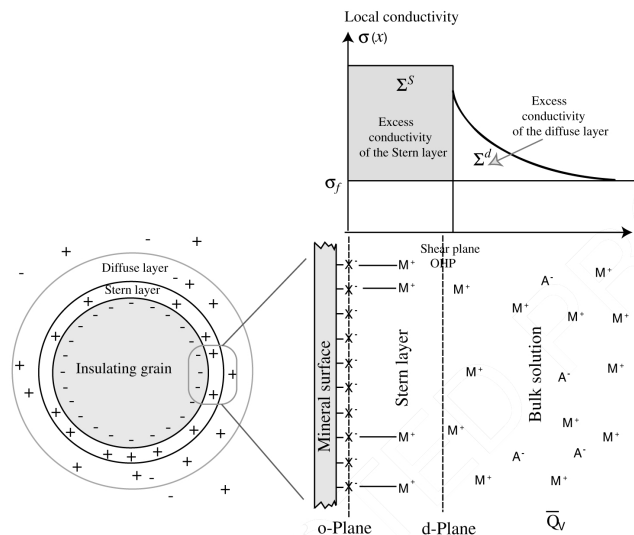
$$\vec{\nabla} \cdot (-\sigma \vec{\nabla} \psi + \vec{J}_s) = 0 \quad (2.12)$$



(a) Image courtesy: Boleve [2009].



(b) Image courtesy: Sheffer [2002].



(c) Image courtesy: Revil and Florsch [2010].

Figure 2.1: (a) schematic representation of the pore space between two grains in a porous medium; (b) schematic view of conduction and convection vectors under flow in a porous medium; (c) A sketch showing the Stern and the diffuse layers. It also shows the distribution of ionic species in the pore space at equilibrium.  $Q_v$  is the volumetric charge density (in  $Cm^3$  and corresponds to the charge of the diffuse layer).

which evolves into a Poisson equation

$$\vec{\nabla} \cdot (\sigma \vec{\nabla} \psi) = \vec{\nabla} \cdot \vec{J}_s \quad (2.13)$$

with

$$\vec{\nabla} \cdot \vec{J}_s = \vec{\nabla} \cdot (\bar{Q}_v \cdot \vec{u}) \quad (2.14)$$

where  $\vec{J}_s$  is the source term for Darcy's flow induced streaming potential. The potential that is measured at the surface can now be written as

$$\vec{\nabla} \cdot (\sigma \vec{\nabla} \psi) = \vec{\nabla} \cdot (\bar{Q}_v \cdot \vec{u}) \quad (2.15)$$

### 2.3.4 Unsaturated flow

For unsaturated flow the derivation is analogous and results in a total current density (compare to Equation 2.10):

$$\vec{J} = -\sigma(S_w) \vec{\nabla} \psi + \frac{Q_v}{S_w} \vec{u}(S_w) \quad (2.16)$$

where

$$\vec{u}(S_w) = -\kappa(S_w) \vec{\nabla} h \quad (2.17)$$

and where, according to Archie's law [Archie, 1942]

$$\sigma(S_w) = \sigma_f \phi^m S_w^n \quad (2.18)$$

where  $\sigma_f$  is the electrical conductivity of the fluids,  $\phi$  the porosity,  $S_w$  the saturation of the porous medium and  $m$  and  $n$  the Archie's exponents.  $m$  is the cementation exponent (with values usually in the range of 1.8-2.0) and  $n$  the saturation exponent (usually with values close to 2). The total current density then consists of

$$\vec{J} = -\sigma_f \phi^m S_w^n \vec{\nabla} \psi - \frac{Q_v}{S_w} K(S_w) \vec{\nabla} h \quad (2.19)$$

where the electrical conductivity of the fluids,  $\sigma_f$  can be represented by

$$\sigma_f = e C_f (\beta_+ + \beta_-) \quad (2.20)$$

in which  $e$  is the elementary charge of an electron,  $C_f$  the ion concentration in the pore fluid and  $\beta_{\pm}$  the mobility of the ions in the fluid, which is dependent on the temperature according to

$$\beta_{\pm}(T) = \beta_{\pm}(T_0)(1 + \alpha_f(T - T_0)) \quad (2.21)$$

## 2.4 Direct Current Resistivity

DC resistivity has been widely used to investigate the subsurface. The applications of DC resistivity vary from studies into the subsurface on waste disposals [Aristodemou and Thomas-Betts, 2000; Binley and Daily, 2003], to testing geomembrane liners [Binley and Daily, 2003], to groundwater contamination studies [Buselli and Lu, 2001], to testing slope

stability [Marescot et al., 2008], to detecting seepage paths in earth dams [Panthulu et al., 2001], to geothermal exploration [Ward and Sill, 1982] and many more. For more information about DC resistivity and a clear introduction to direct current resistivity in geophysics, we refer to Herman [2001].

The mathematical derivation of the direct current resistivity methods starts with the very basics of electrical physics: Ohm's Law [Rubin and Hubbard, 2005].

$$\hat{J} = \sigma \vec{E} = \frac{1}{\rho} \vec{E} = -\frac{1}{\rho} \vec{\nabla} V \quad (2.22)$$

where  $\hat{J}$  is the current density vector,  $\sigma$  the effective conductivity of the bulk material in  $[(\Omega.m)^{-1}]$  (and thus the reciprocal of the bulk effective resistivity,  $\rho$ ),  $\vec{E}$  the electric field vector, in V/m and  $V$  the measured electrical potential.  $\sigma$  consists of two components, the solid phase conductivity ( $\sigma_s$ ) and the fluid phase conductivity ( $\sigma_f$ ), in this manner:

$$\sigma = \frac{(\sigma_f + \sigma_s)}{F} \quad (2.23)$$

where  $F$  is the formation factor.

Following Archie's Law [Archie, 1952, 1950, 1947, 1942; Glover, 2010], the formation factor is defined as

$$F = \frac{\sigma_f}{\sigma} = \frac{\rho}{\rho_f} = \phi^{-m} \quad (2.24)$$

where  $\rho_f$  is the fluid resistivity and  $m$  Archie's cementation exponent, that usually lies between 1.8 and 2.0. The bulk conductivity is now, just like in Section 2.3, dependent on the fluid conductivity (which in turn is dependent on the temperature), the porosity and the water saturation, defined by Archie [1942]:

$$\sigma = \sigma_f \phi^m S_w^n \quad (2.25)$$

The electrical conductivity of the solid phase depends on two factors: the ion mobility factor  $\beta_s$  and the mobility of ions in the double layer.

$$\sigma_s = \beta_s Q_v \quad (2.26)$$

where

$$\beta_s(T) = \beta_s(T_0)(1 + \alpha_s(T - T_0)) \quad (2.27)$$

Combining Equation 2.22, Equation 2.24, Equation 2.25 and Equation 2.26 results in a bulk conductivity that is defined as

$$\sigma = \frac{1}{F} S_w^n \left( \sigma_f + \frac{\beta_s Q_v}{S_w} \right), \quad \text{with} \quad 0 \leq S_w \leq 1 \quad \text{and} \quad 1.8 \leq n \leq 2.0$$

When a direct current is now injected through  $C_1$  and  $C_2$  (in Figure 5.4), the electrical potential,  $\vec{\nabla}^2 \psi$ , is a Poisson equation:

$$\vec{\nabla}^2 \psi = -\frac{J_s}{\sigma} \quad (2.28)$$

where  $J_s$  is the volumetric current source density. The local potential field at distance  $r$  from the middle between the injecting electrodes ( $C_1$  and  $C_2$  in Figure 5.4), is now

$$\psi(r) = \frac{I_s}{2\pi\sigma} \frac{1}{r} \quad (2.29)$$

where  $I_s$  is the injected, or induced current. The apparent (not real, we need inversion to retrieve real electrical potentials) potential difference, measured through electrodes  $P_1$  and  $P_2$ , is

$$V = \psi(P_1) - \psi(P_2) = R \cdot I_s \quad (2.30)$$

where  $R$  is

$$R = \rho g = \frac{\rho}{2\pi a} \quad (2.31)$$

and the distance  $a$  in (Figure 5.4) is defined as

$$a = \frac{I_s}{2\pi\sigma} \quad (2.32)$$

## 2.5 Induced Polarization (IP)

Induced polarization is a method that measures a secondary, relaxation, potential after polarizing the subsurface with an induced current [Rubin and Hubbard, 2005; Patella and Schiavone, 1977; Titov et al., 2002; Slater, 2007]. In time domain IP measurements a direct current (DC) is subjected to (an array of) electrodes on the surface. After a certain time, when the surface has had enough time to charge under the subjected electrical current, the induced charging is stopped and the measure of decay of charge (or relaxation time  $\tau$ ) is the chargeability of the subsurface. This chargeability is a function of the separate chargeabilities of the lithology and the pore fluid (in combination with its dissolved matter) [Rubin and Hubbard, 2005]. Together they produce the total chargeability of the porous medium.

Induced polarization relies on essentially three polarization phenomena:

- the presence of metallic particles
- polarization of the electrical double layer coating the grains
- Maxwell-Wagner polarization

Metallic particles can move around through the pore fluid and by arranging themselves, they are charged. The grains, if they are not completely inert, can be polarized by an induced current. When grains are insulating, Maxwell-Wagner polarization occurs [Wagner, 1914; Sillars, 1937].

The electrical field, after stopping the injection of current and during relaxation time is derived as

$$\frac{d\psi}{\psi} = -\frac{dt}{\tau} \quad \longrightarrow \quad \psi(t) = \psi_0 e^{-\frac{t}{\tau}} \quad (2.33)$$

where  $\psi$  is the electric potential field,  $\tau$  the total time it takes to electrically discharge the medium (or relaxation time),  $t$  is time and  $\psi_0$  the reference electrical potential field before

the moment the induced current is shut off, or the primary potential field. The chargeability  $M$ , is now defined as

$$M = \frac{\delta\psi_s}{\delta\psi_0} \quad \text{in} \left[ \frac{mV}{V} \right] \quad (2.34)$$

where  $\psi_s$  is the secondary potential field during relaxation. This assumes that the electrical energy that is put into the subsurface during induced polarization, is completely discharged during relaxation time. The chargeability can also be measured during only a certain time window of relaxation. Then the chargeability is

$$M_{t_i, t_{i+1}} = \frac{1}{\delta\psi_0(t_{i+1} - t_i)} \int_{t_i}^{t_{i+1}} \delta\psi(t) dt \quad \text{in} \left[ \frac{mV}{V} \right] \quad (2.35)$$

where  $\psi(t)$  is the decaying voltage,  $t_i$  and  $t_{i+1}$  is the beginning and end time of the interval that is measured, and  $\psi_0$  is the voltage measured before the induced current is turned off. The terminology refers to Figure 2.2.

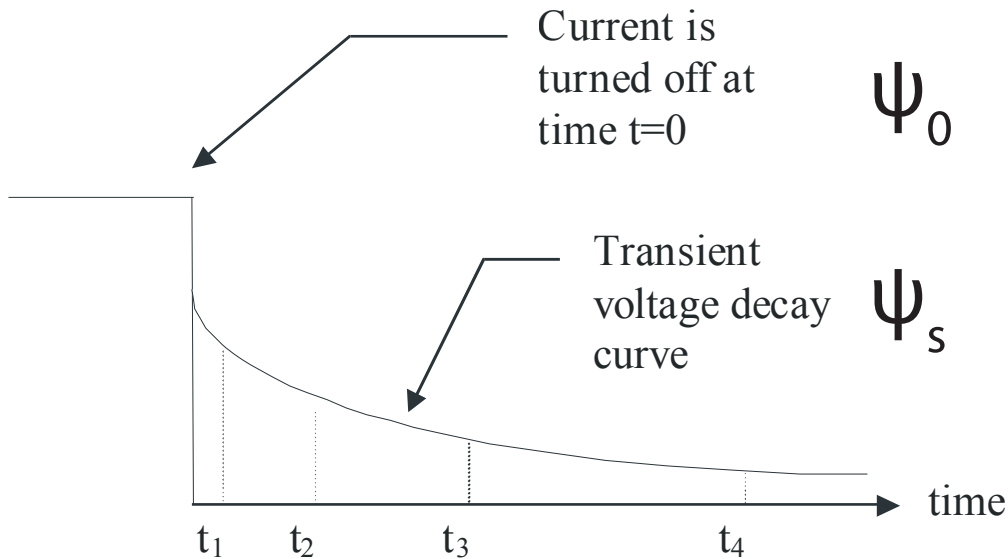


Figure 2.2: The IP decay curve. The chargeability is measured as the area between two time values. For example  $M_{20,40}$  represents the chargeability measured in the interval between 20-40 msec. The delay before the measurements starts are denoted by  $t_D = t_1$ . This figure was taken from the ABEM SAS 1000 / 4000 manual document.

The ABEM SAS 1000 / 4000, the apparatus used to measure DC resistivity and induced polarization in these experiments, measures the time-domain chargeability ( $M_{t_i, t_{i+1}}$ ) defined in the following way:

$$M_{t_i, t_{i+1}} = \frac{1}{\delta\psi_0} \int_{t_i}^{t_{i+1}} \delta\psi(t) dt \quad \text{in} [msec] \quad (2.36)$$

For further reference on the chargeability, see e.g. [Parasnis, 1997, chapter 5].



---

# 3

## Experimental setup

This chapter introduces the equipment that was used, the experimental setup; how it was built and what materials were used. Because the electrodes, the acquisition apparatus and array layouts are different for the transient SP experiment and the steady-state DC resistivity and IP experiments, this chapter does not discuss sensor placement. A rundown of how and where sensors were placed for each experiment will be explained in the section discussing the experiments individually (in Chapter 4 and Chapter 5, respectively for the self-potential and DC resistivity).

### 3.1 Equipment & setup

In order to study the coupling between hydraulic and electric phenomena in porous media in a controlled environment, a lab approach was chosen. A regular fish aquarium (sized L x W x D: 120,7 cm x 44,1 cm x 51,0 cm) served as a container for the porous medium that was going to be created. Since it was needed to be able to adjust head levels at both sides of the tank, water reservoirs were created by placing two silk screens (used in printing industry and available in custom sizes)<sup>1</sup> inside and over the width of the tank (see Figure 3.3, where at the sides the silk screens are visible). These silk screens consist of a wooden frame, held together by glue and a single nail on each corner, and a silk lining that was glued to the frame. A pitch size for these screens was carefully chosen, so the sand would not be able to penetrate through and the water was able to flow freely. The standard sized frame that was purchased did not fit the tank, so they needed adjustment. Cutting off half a centimetre on each side exposed even more of the nails holding the wood together. In order to avoid undesired polarization of these metals nails in the experiments, the frames were spray painted with black rubber paint, which insulates the metal from the aquifer. Two notches in the reinforcing plastic along the top of the aquarium were needed to hold each screen in place. After insertion into the tank on approximately 10 cm from the sides of the tank, the edges were caulked, so, during the experiment, the moving pore water would not cause any sand to enter the water reservoirs.

All sand, that was used to fill the tank, was obtained from the company Rio Grande.<sup>2</sup> According to [Sakaki and Komatsu \[2007\]](#), they have several facilities around the USA and Canada, which may have slightly different hydraulic properties. So it is important to mention

---

<sup>1</sup> Available from Victory Factory Inc., 184-10 Jamaica Ave., Hollis, NY 11423. [www.victoryfactory.com](http://www.victoryfactory.com).

<sup>2</sup> Rio Grande, Co., Building Materials Division, 201 Santa Fe Drive Denver, CO 80223

that the sand that was used here, has been produced at UNIMIN Corp.'s Emmett facility in Idaho, USA. Rio Grande carries their sands in different grain sizes. Hydraulic parameters such as hydraulic conductivities, porosities and particle sizes were empirically obtained (see Sakaki and Illangasekare [2007]; Sakaki and Komatsu [2007]; Schroth et al. [1996] and technical data sheets from Unimin Corporation [1997]). The uniformity coefficients have also been calculated. These coefficients are given by:

$$CU = \frac{d_{60}}{d_{10}} \quad (3.1)$$

where  $d_{60}$  and  $d_{10}$  represent the grain diameter in millimetres of the 60<sup>th</sup> and 10<sup>th</sup> percentile respectively [Kirsch, 2006, Chap. 15]. If the CU is 1, all grains have the same size (the grain size distribution is narrow). With increasing CU numbers, the grain size distribution becomes wider. The Unimin Corp. sands have a uniformity coefficient between 1.4 and 1.9. Other parameters derived by Sakaki and Illangasekare [2007]; Sakaki and Komatsu [2007]; Schroth et al. [1996] were later used for forward modeling in Section 4.4 and can be found in Table B.1.

Three sands of different grain sizes were used in the setup (see Figure 3.1) for these experiments. As a bulk material a medium grained sand (Unimin's Granusil #30) was used. Two columnar compartments were filled with each a different grain size. A rectangular column was filled with a coarser material (Granusil #8) and a square column with a finer material (Granular #70), as shown by Figure 3.1. A simplified geometry was chosen for simplicity in later modelling and inversion.

In Figure 3.2 one can see that the columns of differing grain sizes were constructed using metal casings. Every layer was brought to place in the following manner. The tank was filled with a layer of medium sand and saturated. Subsequently the metal casings were pushed into the medium sand and the inside was dug out. Then this space was filled with either coarse or fine sand and the new sand was also saturated. The following step was to raise the metal shielding and fill the tank with another layer of medium sand. This sequence was repeated until the intended height was reached. The metal shielding made it easier to construct straight columns in angular shapes. The columns were designed to run from top to bottom through the tank, giving the system a vertical symmetry (except for a 3 cm thick layer of #30 sand covering the whole tank, see Figure 3.1). Figure 3.3 shows the columns after removing the metal shielding. The columns were constructed while filling the tank with the medium sand and in layers.

Experience from former experiments<sup>3</sup> learned that a coarse sand loses its residual pore water so easily, resulting in very little residual pore water when the hydraulic head is decreased. The reliability of the electric coupling between the porous material and the non-polarizing sensors is reduced and equipment readings can become unreliable. In this experiment this could have been the case for the coarse sand column in the experiment setup. To be able to keep enough residual pore water at the electrodes, a 3 cm thick top layer of medium sand (same grain size as medium sand bulk material) was placed on top of the whole geometry, covering both columns as well as the medium sand bulk material. Figure 3.1 shows this top layer in its side view. The lightest grey section of 15 x 15 cm is the fine sand column, where the darkest grey (15 x 21.5 cm) indicates the coarse sand column

---

<sup>3</sup>personal communication, André Revil and William Woodruff

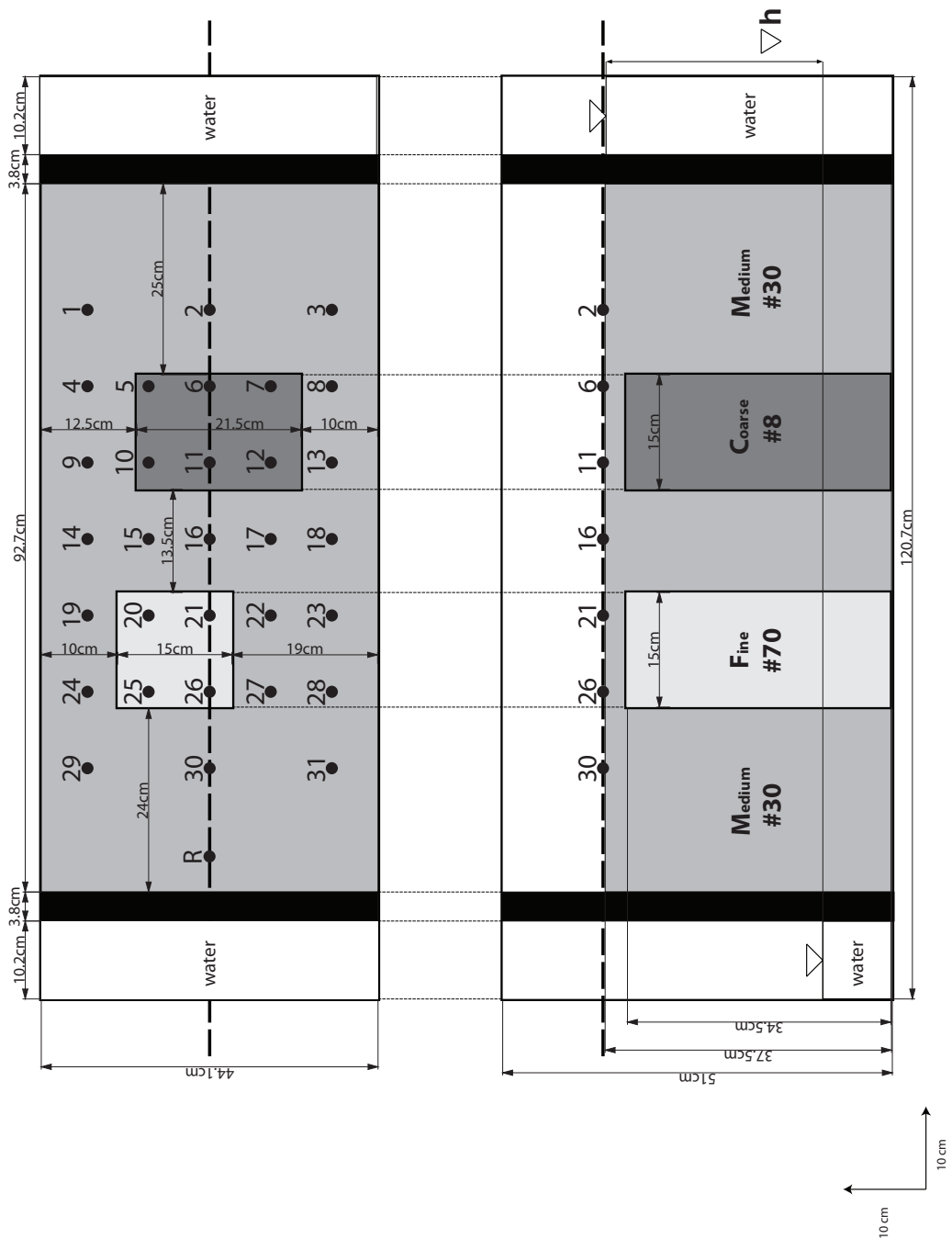
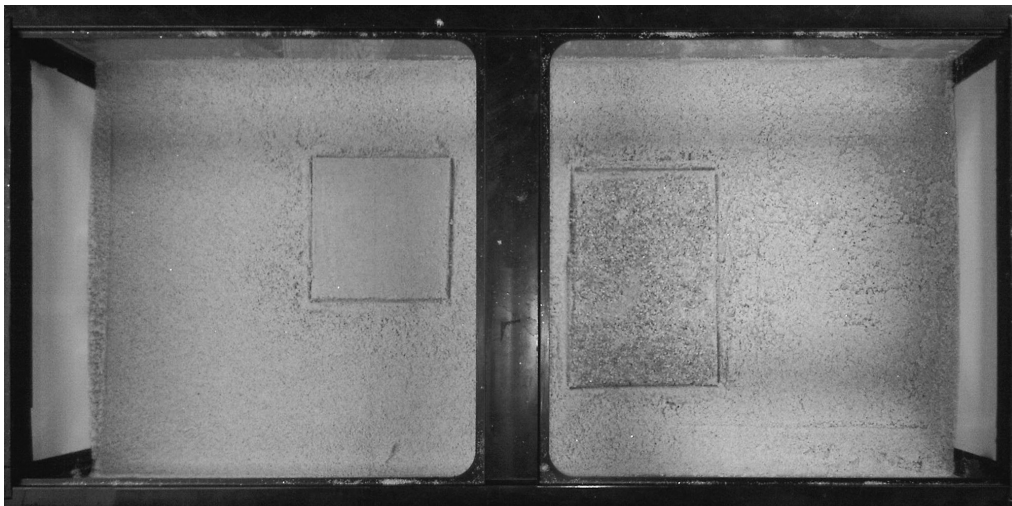


Figure 3.1: Schematic figure showing the sand box setup as used for the SP experiment. The upper figure is a top view, the lower a side view, along the long side and through the middle of the tank. Note the different grain sizes and the head difference between the two water reservoirs. The numbers represent sensor locations for the SP experiment. The dashed line through the middle is where the cross section (below) was taken. This figure is to scale.



*Figure 3.2: A view of how the sand columns were constructed, using metal shields to prevent the sides to collapse in unstable saturated sand.*



*Figure 3.3: Upon completion, this is what the sand columns look like. Top view. The black bar in the middle is part of the plastic reinforcement that runs along the edges of the tank and is meant to increase its structural integrity.*

and the middle grey bulk is the medium sand. 'Water' indicates the water reservoirs and the two thick black lines represent the frame of the silk screens. The actual silk lining is on the inside of this frame, facing the porous medium and away from the water reservoir.

Note that the long sides confining the artificial porous medium consist of glass and thus they are electrical insulators. An insulator will cause the electrical current density to reflect off of it, very similar to how a surface wave in water reflects off of the side of the reservoir, or more general, off the confining element. The short sides, however, are electrically continuous; a transition from a saturated porous material to a water reservoir. The porous medium and the water reservoir have very different (electrical) properties though and will cause the electrical current density electrical current density to diverge in the water reservoir. Whether measurements are active (resistivity) or passive (self-potential), electrical current travelling from a source to a receiver, will be influenced by these barriers.

After completing the setup, the sand was saturated until complete saturation was accomplished. For several hours clean tap water was put into the system in a reservoir on one side and drained from the reservoir on the other side of the tank. This was done to remove any dust and dirt from the sand, to avoid their influence on the experiments.

---

## 4

# Transient experiment: Self-Potential (SP)

## 4.1 Introduction

Highly sensitive self-potential measurement equipment has proven to be able to measure indicators for differences in flow velocities in underground water reservoirs [Sill, 1983; Jardani et al., 2007; Suski et al., 2004; Minsley et al., 2007a; Panthulu et al., 2001; Jardani et al., 2006] and in recent studies, SP has also been used to monitor the chemically active boundaries of contamination plumes in subsurface water [Buselli and Lu, 2001; Revil et al., 2009; Arora et al., 2007; Minsley et al., 2007b; Mainault et al., 2006, 2005] and the chemically active edges of ore bodies [Mendonça, 2008]. SP has also been used for the detection and localization of hydromechanical disturbances in lab setups [Crespy et al., 2008] and in dam seepage monitoring [Panthulu et al., 2001; Rozycki, 2009; Rozycki et al., 2006; Moore et al., 2010; Boleve et al., 2009].

The different sands, that were used in the tank setup (see Section 3.1 for more information), have different hydraulic parameters. This should show up as a velocity anomaly in the velocity field in the tank during transient flow experiments. For this transient SP experiment the central question can be formulated as: using a two-dimensional grid of surface sensors and highly sensitive equipment can we recover the geometry of predefined sand bodies in the tank setup?

## 4.2 Methods

The tank setup as explained in Section 3.1 was used to perform these self-potential experiments. In order to have a flow experiment, a hydraulic head difference was applied to the tank. Two experiments were performed: one with 19 cm and one with 9 cm hydraulic head difference. The system was closed, meaning that, during the experiment, no water goes out of or comes into the system. This was done to decrease possible changes in the electrical conductivity of the pore fluid, because, especially in spring, the Colorado tab water's electrical conductivity can change significantly.

Variable	Value experiment # 1	Value experiment # 2	Unit
T	21,9	22,3	$^{\circ}C$
$\sigma_w$	180,5	176,0	$\mu S$
pH	7,44	7,57	$-\log_{10}$
$\Delta H$	19 (?)	9	cm
Pumping speed	600	300	rpm
Discharge	+/- 2,0	+/- 1,0	L/min

Table 4.1: Parameter values under which Experiment 1 and 2 respectively were performed.

### 4.2.1 Pump

In order to get the desired hydraulic head difference, a simple system of a pump and a hose (5 m of hose between pump and tank on both sides, in order to minimize noise by vibrations), pumped water from one water reservoir to the other, located on opposite sides of the tank (see Figure 4.1a). When the pump was started, a hydraulic head difference was created. This hydraulic head difference is directly related to the discharge  $Q$  (see Figure 4.1a), which is the pumping speed in this experiment (Figure Table 4.1 for measurement parameters during both experiments). After turning it on, the pump was left pumping for several hours to make sure the whole system had come to a steady-state flow equilibrium and also to allow the partially saturated zones to adjust. A peristaltic pump<sup>1</sup> was chosen, in order to decrease electrical noise from the pump in the adjustment phase. Even though the pump was turned off during the actual experiment, a lower-noise pump was required when checking whether the electrical measurement equipment had come to an equilibrium. In a peristaltic pump, the water is driven through a flexible rubber hose by a rotating wheel with a few discs (see Figure 4.1b for an example). The advantage of using a peristaltic pump is that the pump itself is electrically insulated from the water, thus avoiding the introduction of electrical noise. It turned out that these types of pumps still introduce some noise, but that is probably due to oscillation in the hose. This slight movement in the water column causes a small self-potential signal. This noise can be seen in Figure 4.3, in the first 243 seconds. For this particular experiment, the noise was not a problem, since the pump was turned off at the start of the actual experiment (the recovery phase).

<sup>1</sup>Peristaltic pumps are available for rent from Geotech Environmental Equipment, Inc., 2650 East 40th Avenue Denver, Colorado 80205. [www.geotechenv.com](http://www.geotechenv.com).

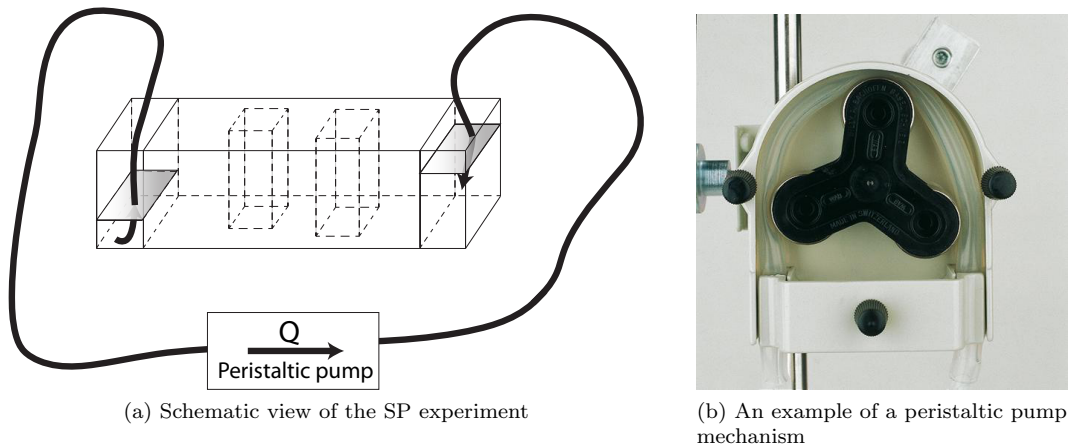


Figure 4.1: (a) A schematic view of the transient SP experiment, as described in Section Chapter 4. The peristaltic pump pumps water from the left reservoir to the water reservoir on the right, creating a hydraulic head difference between both ends. (b) An example of a peristaltic pump. This is not the actual pump that was used in these experiments. Image courtesy: Eijkelkamp Agrisearch Equipment ([www.eijkelkamp.com](http://www.eijkelkamp.com)).

## 4.2.2 Electrodes

Thirty-two sensors were used to record the self-potential signal, produced by the flow of water in the porous medium. These sensors are amplified Ag-AgCl non-polarizing electrodes that are widely used in medical applications and research, such as EEG (electroencephalography, to study brain activity), ECG (electrocardiography, to study activity of the heart), EGG (electrogastrography, to study bowel activity) and EMG (electromyography, to study muscle function) measurements.<sup>2</sup> They have an input impedance of  $300\text{ M}\Omega$ . Previous experiments [Haas and Revil, 2009] showed that the advantage of these electrodes is that they provide an affordable solution to measure an electric signal with low offset voltages at a good signal-to-noise ratio. They also have reasonably stable DC performance. Another advantage of these electrodes is that they are small (less than 1 cm in diameter): point measurements are possible on relatively small scale models.

<sup>2</sup>These electrodes and all other necessary equipment and software is available from Biosemi ([www.biosemi.com](http://www.biosemi.com)), started by the Medical Physics department of the University of Amsterdam in 1998.



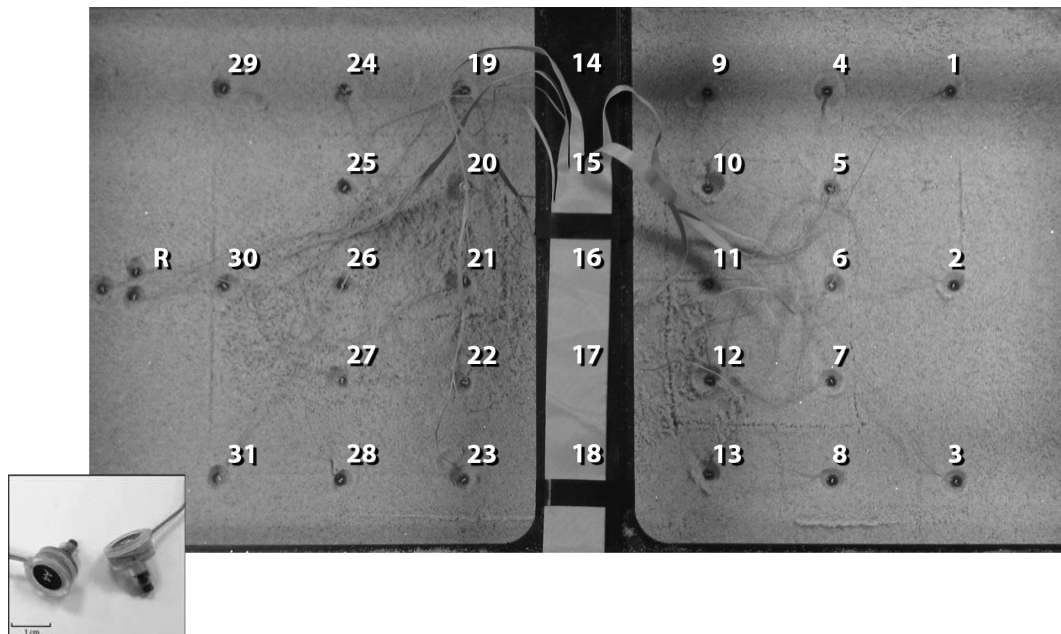


Figure 4.2: Top view of the experimental tanks, just after installing the non-polarizing Ag-Cl electrodes and just before covering them up with a small layer of sand. These electrodes were placed just below the surface to ensure good electrical coupling with the porous medium. Sensors 14-18 are not visible due to the reinforcement bar of the tank. The inset is an example of two Biosemi Ag-AgCl, amplified, non-polarizing electrodes.

### 4.2.3 Acquisition system

The acquisition system is the same as was used by Haas and Revil [2009]; Crespy et al. [2008] and consisted of: a battery powered, self-contained, galvanically isolated, digitally multiplexed, high sensitivity voltage measurement system. It has a single analog to digital converter per measurement channel and was used in combination with the amplified, non-polarizing, Ag-AgCl electrodes. These active electrodes have very low output impedance and therefore all problems with regards to capacitive coupling between the cable and sources of interference are eliminated [Crespy et al., 2008]. As further described by Haas and Revil [2009], in order to avoid interference from noise sources with the measurements, the raw signals from the Ag-AgCl electrodes are digitally multiplexed and serialized into a bit wide data stream, which is subsequently transmitted through a fiber-optic cable to a device that handles the USB-computer interface. The fiber-optic cable is used to achieve galvanic isolation, reducing outside noise even more.

### 4.2.4 Electric coupling and reference electrode

All electrodes were buried just below the surface, in order to ensure sufficient electric coupling between the electrodes and the porous medium. Figure 3.1 and Figure 4.2 show the locations of each electrode and also shows that 31 electrodes were used to record the self-potential signal. 1 Electrode was used as a reference (marked R in the figure); all measured results are referenced to this electrode. In Figure 4.2 can be seen that the electrodes were buried just below the surface. After inserting the electrodes, they were buried with sand, to ensure a

reliable electric coupling between the electrodes and the porous medium. This would further increase the reliability of the measurements. Refer to Section 4.3 for the resulting data.

## 4.3 Resulting data & data processing

### 4.3.1 Raw data

The resulting data include several sources of noise. Some processing steps were taken in order to attenuate these noise sources, making the data set better for comparison with a synthetic data set that came from Comsol<sup>®</sup> modelling (see Section 4.4). The following list the processing steps that were subsequently performed with Matlab:

1. remove gain
2. resample data
3. remove begin and end of data
4. least squares polynomial curve fitting
5. remove resulting polynomial from data

These steps will be explained in the following sections.

### 4.3.2 Removing gain, resampling and reducing the data

Figure 4.3 shows the raw data (in blue). This is the data that comes straight from the Biosemi<sup>®</sup> device. These data have been divided by the Biosemi<sup>®</sup> measurement equipment's gain of 32 and are in mV. The green vertical line indicates the start of the experiment, the moment the pump has been shut off (refer to Section 4.2.1 for an explanation). The subsequent step, resampling the data, removes high frequency noise. A side effect of resampling, is that it gives oscillating effects at the edges of the data and at spikes or sharp increases or decreases. By padding the data on both ends, the edge effects can be reduced, but not completely removed. This why the resampled data only runs from the start of the experiment (at  $t = 244s$ ) until an arbitrary time close to the end of the experiment (at  $t = 1443s$ , to make a nice data set of 1200 samples). This does not yield any implications since there is no interest in the first 243 samples, which are part of the noisy data of pumping to reach the equilibrium. The last 57 samples can also be discarded, because the system has come to a new equilibrium long before the experiment was finished (see Section 4.3.3 for further explanation). The effects at spikes and sharp in- or decreases are not very large. This can be seen in figures 4.3, 4.4, 4.5 and 4.6.

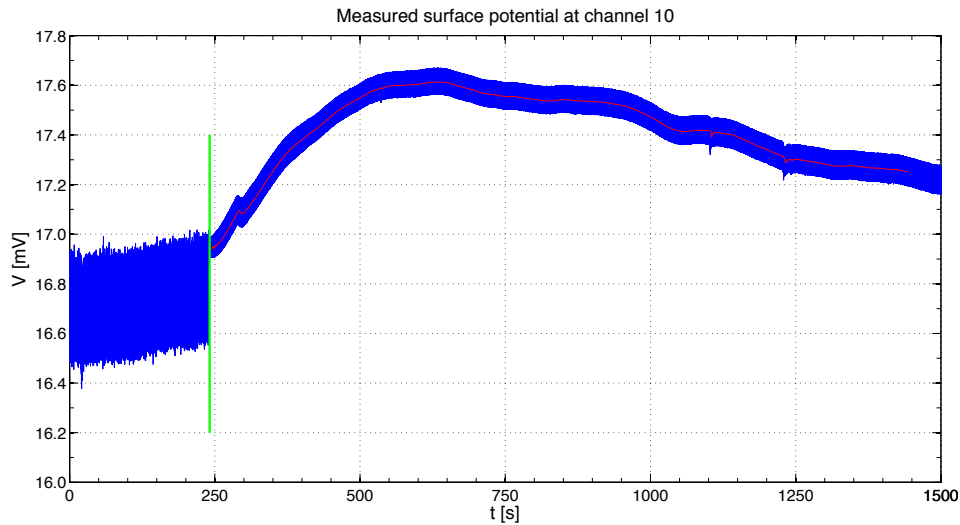


Figure 4.3: Raw data that came from the SP experiments. Here channel 10 is shown as an example. Channel 10 shows a typical electrical response that was measured in both SP experiments. The y-axis shows the measured potential of the channel in microvolts, referenced to the reference electrode. The blue data is the raw data from the Biosemi<sup>®</sup>, divided by the gain of 32, and the red line is after resampling the raw data. The green vertical line indicates the beginning of the experiment, the moment when the peristaltic pump is shut off.

### 4.3.3 Polynomial curve fitting and detrending

The raw data consists of two major contributions: the real SP signal and data from noise sources. From 700 seconds and onwards in the experiment data (see to Figure 4.4), the water levels in the water reservoir on either side of the tank were equal. From this moment,  $\vec{u}$  is very close to zero and thus the contribution of the streaming potential to the data is negligible. All other contributions are assumed to be from background noise sources and should be removed from the data. In order to remove these contributions, a 2<sup>nd</sup> order polynomial has been fit to the data from  $t = 700$  seconds onwards, the polynomial was removed from the data, for each channel separately for the complete time window. This was done with a Matlab least squares method. Removing those polynomials gives the detrended data for each channel. The red line in both Figure 4.4 and Figure 4.5 represents the 2<sup>nd</sup> order polynomial. In Figure 4.5 the reference electrode is obviously 0, since the curve has been subtracted from itself.

Figure 4.6 shows the detrended data for all channels. From the type of experiment and from Figure 4.6 it is clear that the (linearly) coupled system of Darcy's flow and self-potential is diminishing with time. Towards the end of the experiment, let's say at approximately  $t = 700$  s (this is also due to the method of detrending discussed previously in this section), the system has come to an equilibrium and flow goes towards 0. There are also some hiccups visible in the data. Since the measurement equipment is very sensitive, these are most likely due to external disturbances during the experiment, such as people moving around in the room.

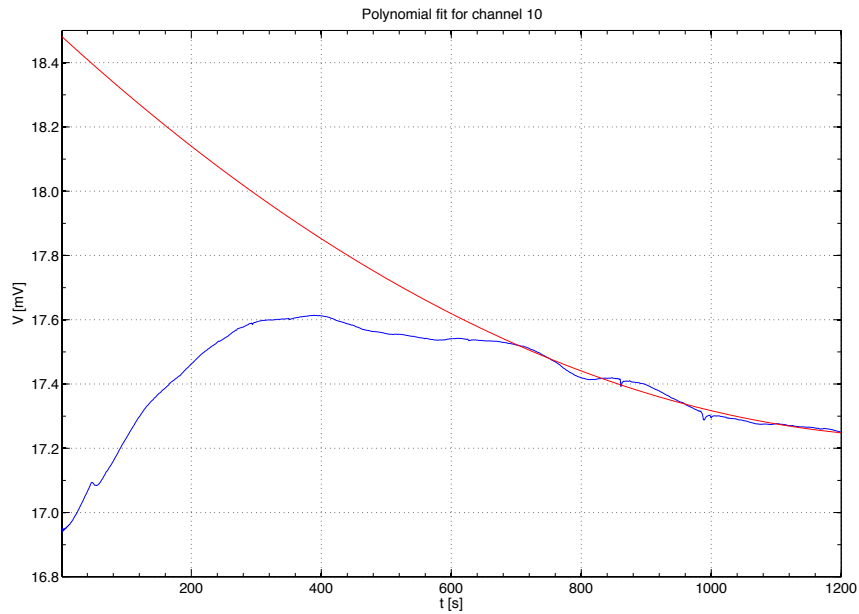


Figure 4.4: The same data as in Figure 4.3, but here, the red curve represents the 2<sup>nd</sup> order polynomial that was fit to the data and will be used to detrend the data, in order to remove low frequency noise.

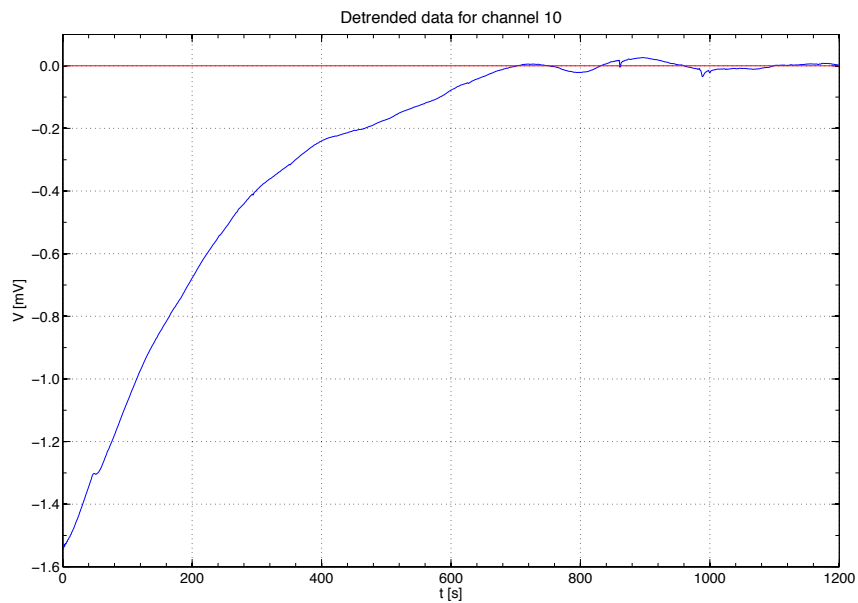


Figure 4.5: Detrended data for channel 10. The red line represents the 2<sup>nd</sup> order polynomial that had been detracted from the data. This is zero, since it has been detracted from itself. The solid blue line is the detrended data in mV.

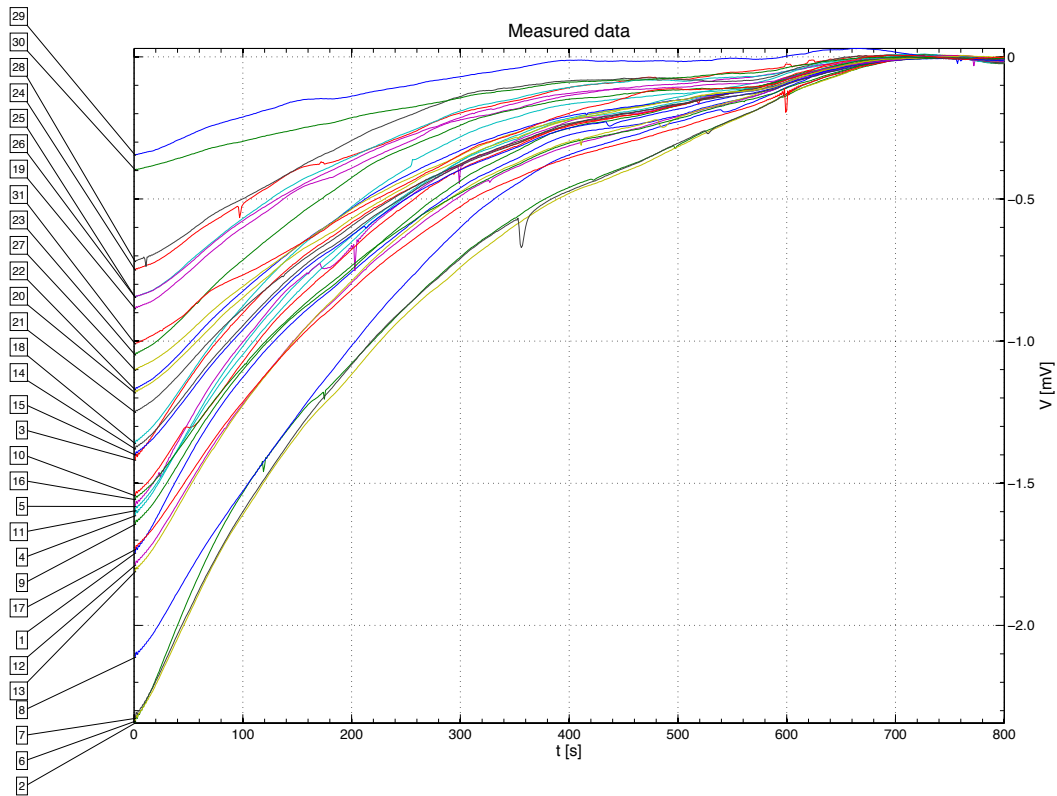


Figure 4.6: The measured data over the first 800 seconds of elapsed time during the experiment. Every line represents the SP signal of a single channel, which are numbered on the left.

The reason that all channels have negative values for almost the complete timespan, is because the reference electrode R is located at the downstream side of the tank. The water flows towards the reference electrode and thus is the referenced self-potential from all electrodes negative. Would the reference electrode be placed on the other end of the tank, or would the flow be of opposite direction, all values would be positive.

Figure 4.6 also shows that channels furthest away from the reference electrode generally have a larger self-potential signal. This is due to the fact that the distance between the reference electrode and those electrodes is larger. A larger distance means there is more of the aquifer in between them and thus there is more pore surface contributing to a larger self-potential signal. In the data processing all data from all electrodes have been referenced to the same reference electrode R, such that the electrodes on the opposite side of the tank have larger final signals. This is very clearly visible in Figure 4.7.

Figure 4.7 shows the same data as in Figure 4.6, but interpolated and extrapolated over the whole tank's surface and for  $t = 75$  s. This was done using the *Kriging Toolbox* in Matlab. Figure 4.8 shows the semivariance for Figure 4.7. A semivariogram, such as Figure 4.8, shows the length of correlation in a spatial data set. This variogram needs to be fitted with a model (the blue line in Figure 4.8). This model is later used to produce the contour plot. This process is called Kriging.

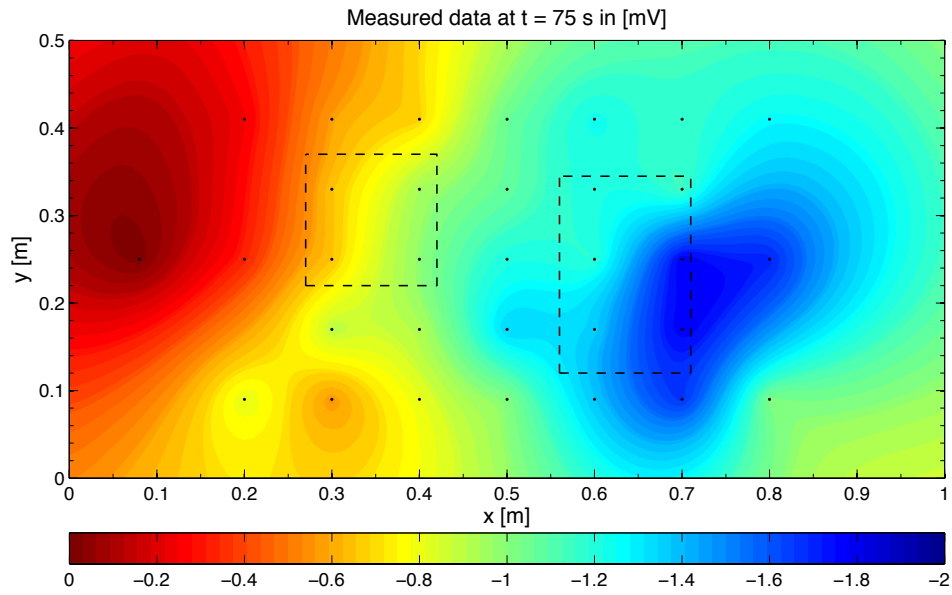


Figure 4.7: A contour plot of the measured data at  $t = 75$ . The color bar shows the value of the surface electrical potential in mV. The effects of the two sand columns, outlined by a dashed line. The contouring was done, using Matlab and the Kriging Toolbox. Figure 4.8 shows the semivariance for the Kriging that was performed for this contour plot.

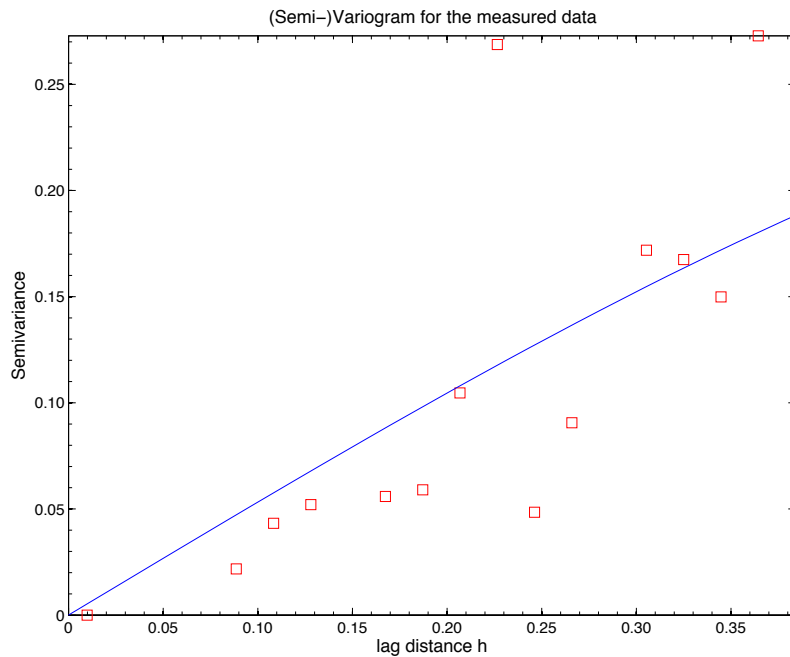


Figure 4.8: The semi-variance for the measured data. The red dots show the semi-variance values. The blue line shows the fit that was used for the Kriging to construct Figure 4.7. This fit is good enough to avoid biasing of the Kriging image.

Note that, due to the extrapolation, contours shown outside of the electrode markers is less reliable. The small markers show the electrode placements, the dashed lines show the outlines of the underlying sand cores and the contours are the local self-potential signal in mV. The outlines of the cores can also be seen in the data: the coarse sand core has somewhat higher values than the surrounding aquifer, where the data seems to be a bit lower in the areas under and left of the square (fine sand) column, although this is not as clear as the outlines of the coarse sand column. The effect of the coarse sand column is larger and of opposite character compared to the fine sand column. One of the explanations for this might be that the coarse sand column has a larger volume and thus has a larger impact on the data.

## 4.4 Forward modeling

A numerical model was developed in order to determine the parameters from the actual real-life SP flow experiment. To model this experiment, sets of partial differential equations, which are derived in Chapter 2, have to be solved. Comsol Multiphysics<sup>®</sup> has built-in solvers capable of iteratively (in time) solving these partial differential equations, for the hydrological as well as the geophysical problem. Comsol exhibits a Richards' module, capable of solving the hydrological problems, the Solute Transport module to model solute transport and the Conductive Media DC module to solve the electrical geophysical model. The Richards' equation module was used to solve the hydrological problem in the saturated as well as the Vadose zone.

To simplify the model and to avoid strange effects at internal borders with large differences in modeling parameters, the water reservoirs on both short ends of the tank were not modeled and the dimensions of the tank were set to 1.0x0.4x0.5 (LxWxH). All sides of the tank were set to 'electric insulation' (electric problem) and 'zero flux' (hydrologic problem) and the top surface to 'air', where all internal faces were set to continuity.

Following the general lines of [Wheaton and Singha \[2010\]](#) and [Wheaton \[2009\]](#), the models use the Direct(PARADISO) solver, in either a stationary or transient mode (the initial value and transient model respectively). To overcome convergence problems, the error tolerance was set to 0.1 and 0.05 for the relative and absolute tolerance. For the initial value modeling, the stationary version of the Direct(PARADISO) solver was used, with all modules set to stationary. For solving the transient model, the time-stepping version of Direct(PARADISO) was used, combined with all modules in transient solving mode. The time steps were taken at specified times (0 to 800 seconds, on every second) and timestepping was set to intermediate (as recommended by [Wheaton \[2009\]](#)).

Table B.1 shows what values were used to solve the equations with Comsol. The variable name column gives the name of the variable as it exists in the Comsol model. Values for these parameters were either taken from the publication that is noted in the table's description, taken from previous experience with modeling these types of experiments or were measured at the moment of the experiment (as indicated in the Description column in Table B.1).

### 4.4.1 Initial values model

The experiment started with initial boundary conditions, as described in Chapter 2. Since the boundary conditions at both short ends of the tank differ from each other, a non-constant hydraulic head distribution throughout the sandbox exists at the beginning of the experiment. In order to have initial values for the hydraulic pressure within the entire domain of the model, a steady-state hydrological model was developed. This model has the

boundary conditions mentioned above and calculates the hydraulic pressure in the whole tank. This is done using the Richards' equation module in Comsol and the values for parameters as described in table Table B.1.

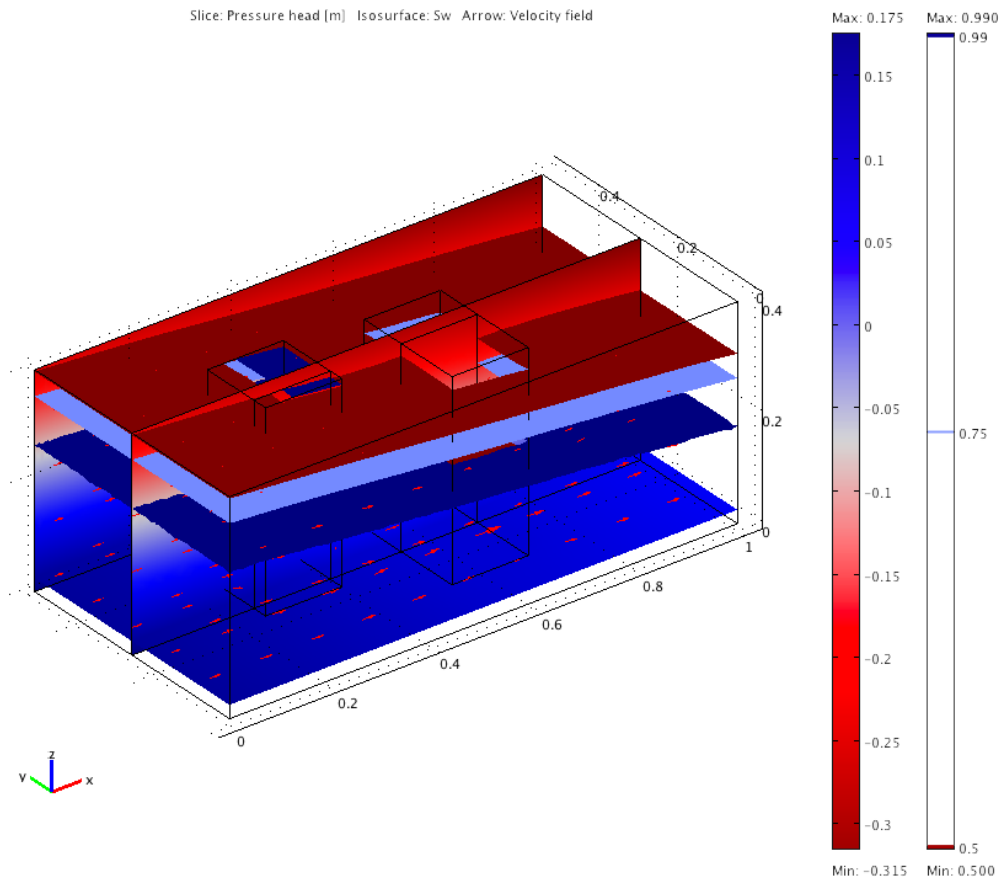


Figure 4.9: Results of the initial subdomain model, that was used as the initial value for transient SP modeling. This model has boundary conditions as mentioned in Table B.1 (26.3 cm for  $x = 0$  and 17.3 cm for  $x = 1$ ). The three isosurfaces, dark blue, light blue and dark red, represent the 100, 75 and 50% saturation levels, the vertical cross-sections the pressure head [m] and the arrows correspond to the relative flow velocity and flow direction.

An example of the results of such an initial value model is displayed in Figure 4.9. The three subhorizontal isosurfaces represent  $S_w$ , or the saturation fraction, where the dark blue, light blue and red isosurfaces mark the 100%, 75% and 50% hydraulic saturation boundaries respectively. The lower horizontal and two vertical planes show the pressure head in [m]. The small red arrows are indicators of flow direction under the mentioned boundary conditions and the size indicates relative flow velocity. Comsol's 'Extrusion coupling variables' function, enables us to couple the values of hydraulic pressure in all subdomains from the solution of the initial values model to the transient model. This means that, after storing the results of the initial values model, they can be used as an initial value when solving the transient model.



### 4.4.2 Transient model

Where the initial values model calculates the initial pressure heads in the whole tank, the transient model was developed in order to solve for the hydrological, solute transport and electrical problem through time, in order to create similar data as were measured in the transient self-potential experiment. Therefore the transient model consists of three components:

1. the **Richards' equation module**, transiently calculating the hydraulic heads and flux due to the initial conditions from the initial value model
2. the **Solute Transport module**, which transiently calculates the transport of ions in the pore fluid due to flow
3. the **Conductive Media DC module**, that transiently solves the electrical potential density problem

These three coupled problems were solved at every time step. In the measured data in Figure 4.5 one can see that after 800s of experimental time, there is hardly any SP signal on the tank's surface anymore. To limit the time it takes to solve the model (modeling time), it was chosen to model 800 time steps of 1s. The solver automatically adjusts the step size to an appropriate stepsize (it needs smaller steps in the beginning, to reduce solving error).

After solving the transient model for the estimated values for parameters such as permeability, electrical conductivity and porosity (Table B.1) was completed successfully, the results were compared with the experimental data. In order to be able to compare both data sets, the modeled data had to be processed. The modeled data had to be referenced to the reference electrode, located at  $R$ , in Figure 3.1. The spontaneous potential for this location was also calculated in the transient model. Subtracting the value for this location from every other electrode at every time step, will generate the actual referenced data at that location. In Figure 4.10, the surface potential contour slice is not representative for the surface electrical potential, since this is a snapshot of the model and thus shows non-referenced values for electrical surface potential. See to Figure 4.12 for a referenced surface potential contour snapshot at  $t=75$  s. That figure was made with data taken from that same model.

Figure 4.11 shows the modeled data for the complete timespan. On closer examination, this figure shows that almost all of the results for the electrodes are grouped in the lines in the  $y$ -direction on the tank's surface. This results in a neat gradient in the data in the  $x$ -direction, as shown in Figure 4.12. The effects of the two sand columns, outlined by a dashed line, is clearly visible. Where the sand is coarser (the right, rectangular column) the contour lines converge, whereas in the finer sand (the left, square column), the contour lines diverge. This is similar to Figure 4.7, although the effects are much clearer, making them more distinguishable.

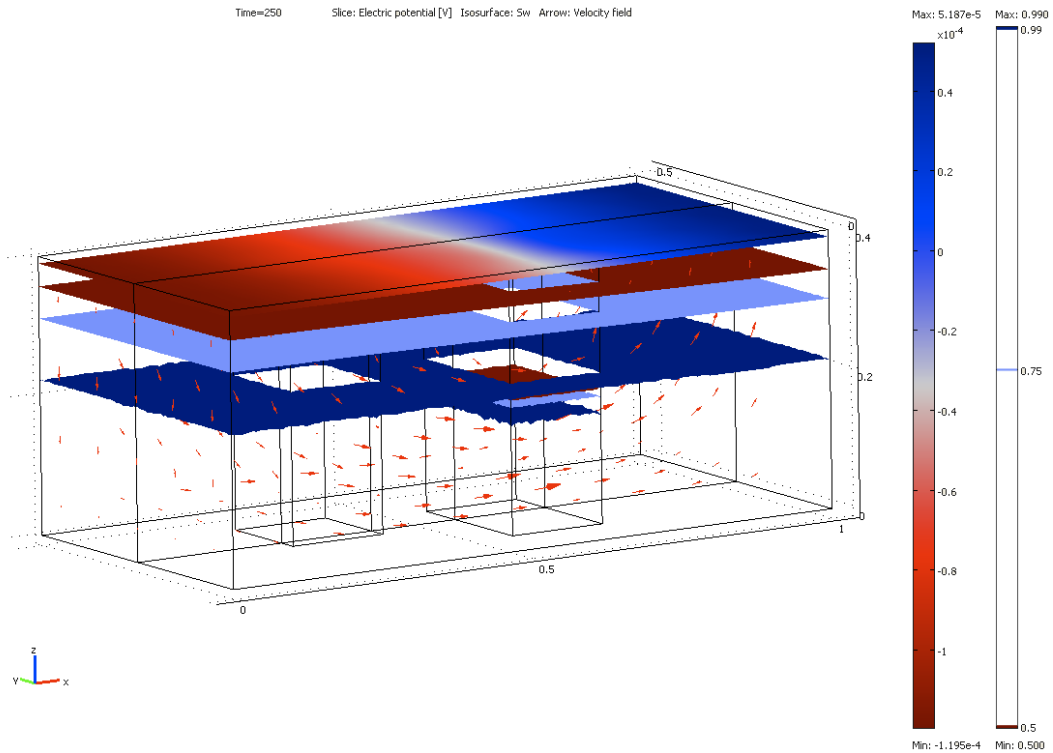


Figure 4.10: A snapshot of the transient model while it is solving. This snapshot was taken at  $t=250$  s. One can see the water saturation at 100%, 75% and 50% levels in dark blue, light blue and dark red isosurfaces respectively. At closer inspection, it is visible that the water saturation levels have not reached equilibrium yet (where  $x=0$  the 100% level is approximately 10% higher than at  $x=1$ ). The arrows indicate flow direction and their size represent relative flow velocity. The contour slice at  $z=0.4$ , with coloured scalebar to the right, represents the actual surface potential at  $t=75$  s. See text for further explanation.

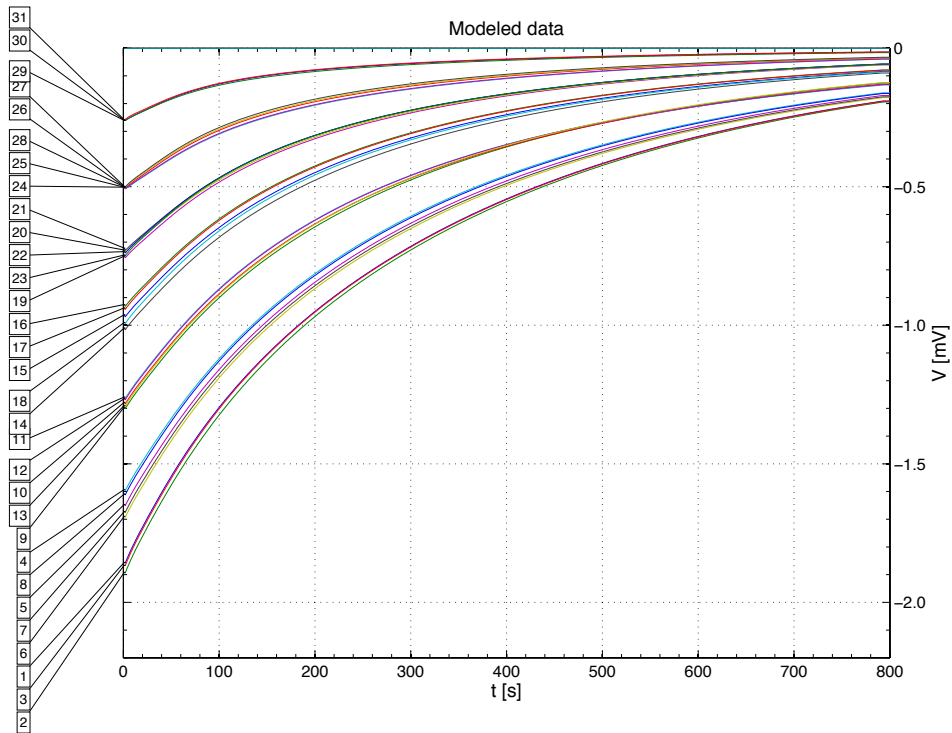


Figure 4.11: This plot shows the complete timespan for the modeled data. The numbers on the left represent the SP sensors (see to Figure 3.1 for exact locations). Compare with the measured data in Figure 4.6.

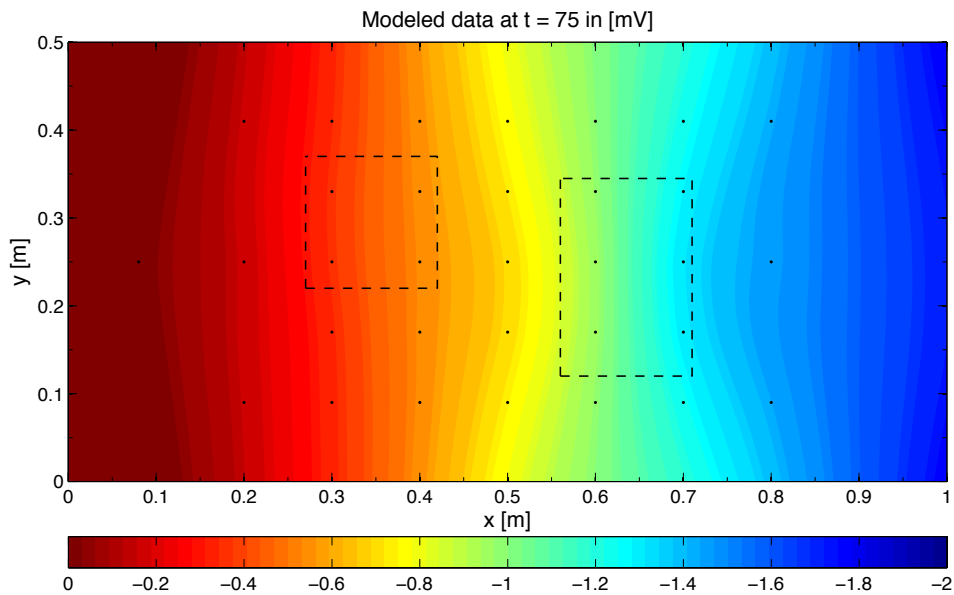


Figure 4.12: A contour plot of the modeled data at  $t = 75$ . The color bar shows the value of the surface electrical potential in mV. The small dots represent the positions of the SP electrodes.

### 4.4.3 Model improvement & data comparison

In an iterative process of trial and error, the model parameters were manually adjusted (simultaneously in both the stationary initial value model and the transient experiment model) in order to give modeling results that are closer to the real-life example experiment. The final result can be seen in Figure 4.13, where the blue lines represent the measured and the red lines the modeled data over the full timespan of 800 s. The self-potential signal is in mV. The model has reasonable resemblance with the actual measured data, follows the general trend and has comparable values for most of the channels. Towards the end of the experimental time, the hydrological system has not come to an equilibrium yet, where the actual tank experiment has. This might be due to the detrending of the actual data, which has not been done on the modeled data. This detrending forces the data to go to zero from 700 s onwards (as described in Section 4.3.3).

For better data comparison between the measured and modeled data, both data sets were plotted in grouped plots for the first 250 s (Figure 4.14 and Figure 4.15). Furthermore, the differences and the linear correlation coefficients of these data sets have been plotted in contour plots in Figure 4.16 and Figure 4.18.

In Figure 4.14 and Figure 4.15, the colors of the data represent the location of the channels, where blue, red and green indicate channels above the No. 8, 30 and 70 (coarse, medium and fine) sands respectively. When comparing Figure 4.14 and Figure 4.15, especially channels 31 and 17 are standing out for being very different in the measured data from the modeled data. It can also be seen in Figure 4.14 that both these channels do not follow the general trend which would be expected when examining the remaining data (the other channels). There might have been a problem with these electrodes or with the electrical coupling between the electrodes and the sand surface. Figure 4.16 and Figure 4.18 show this difference more clearly.

Figure 4.15 shows the data for channels in one line in the y-direction is neatly grouped. It is also visible that the channels in a line in the y-direction that are above one of the two sand columns, stand out from the data from the surrounding channels in that line (refer to channels 4 and 8 compared to channels 5, 6 and 7 in Figure 4.15). This makes it possible to discriminate between the different sand types from the modeled data. In the measured data however, this is much more difficult, because the data are not so neatly curved and grouped as they are in the modeled data and although data processing removed much noise, there is still noise present in the data. Still, the measured data show resemblance with the modeled data (the green lines for instance and channels 29 and 30).

In order to visualize differences more clearly, a surface contour of the absolute differences between the measured and modeled data at  $t = 75$  was plotted in Figure 4.16, where darker colors show larger differences and lighter colors smaller differences. In this snapshot, the differences are largest in between the sand columns (outlined in dashed black lines), especially in channels 6, 7 and 12. Also channel 27 and 31 show larger differences, up to 0.5 mV (at  $t=75$  s).

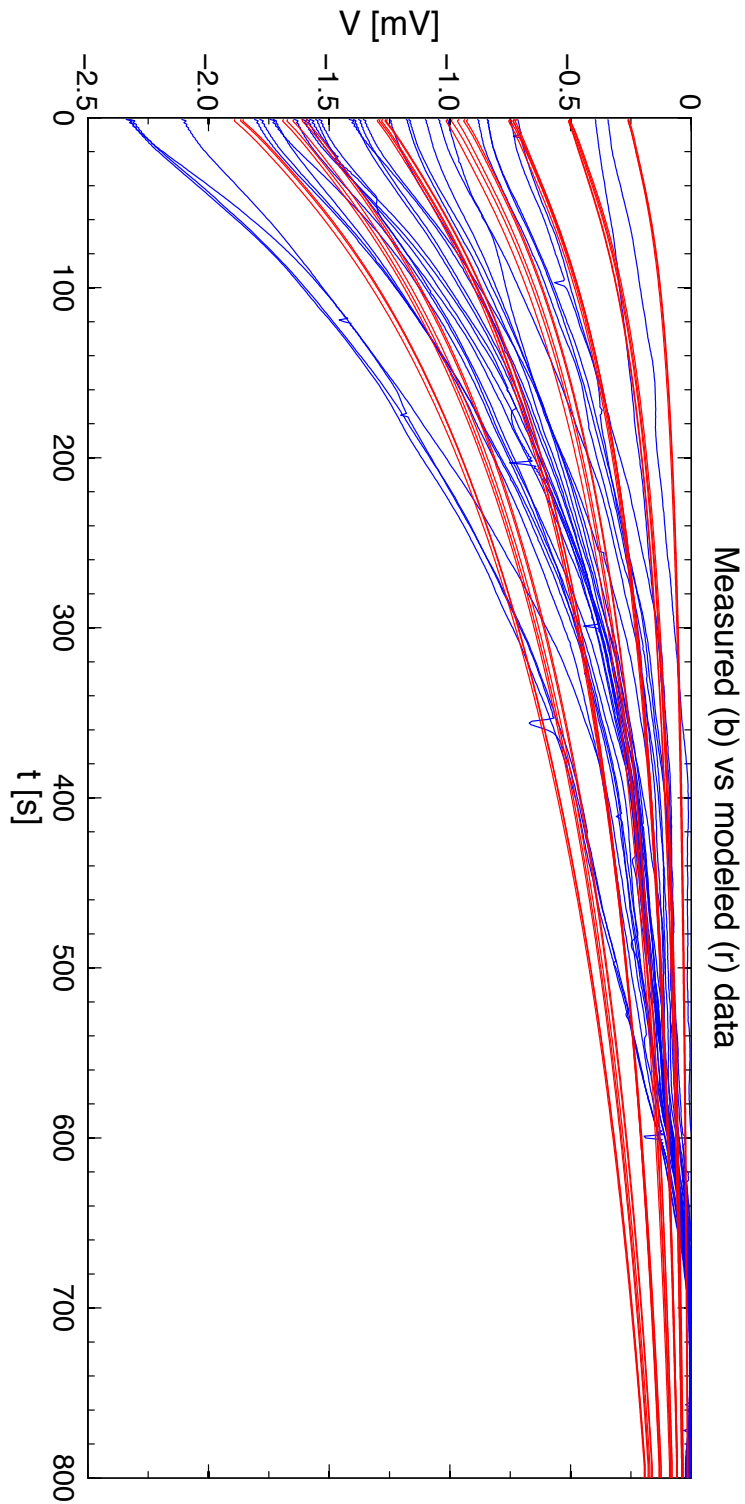


Figure 4.13: This figure shows the measured (in blue) as well as the modeled (in red) data for the complete modeled time window. Self-potential signals are in mV and time is in seconds.

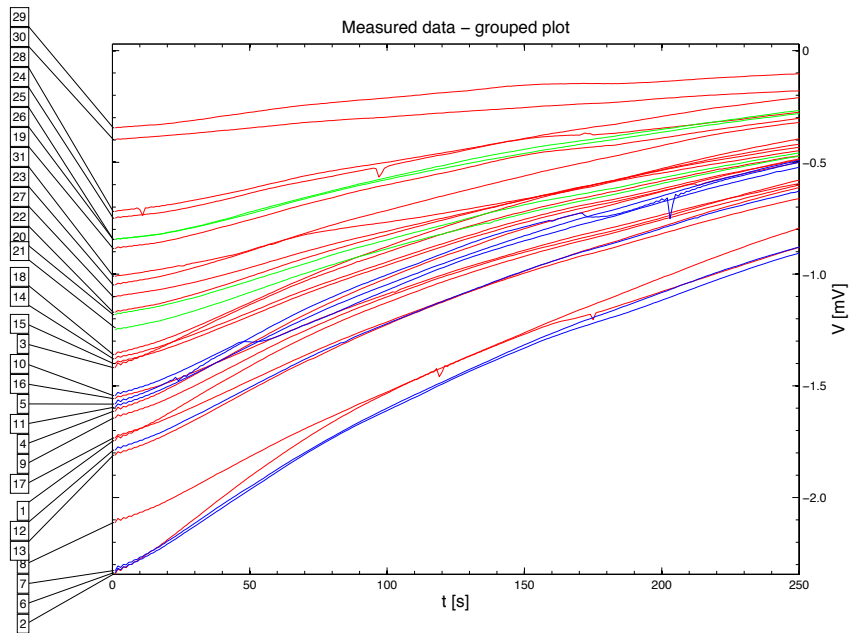


Figure 4.14: This plot shows the first 250 seconds of the experiment, where every line represents the SP signal of a single channel, annotated on the left margin of the figure.

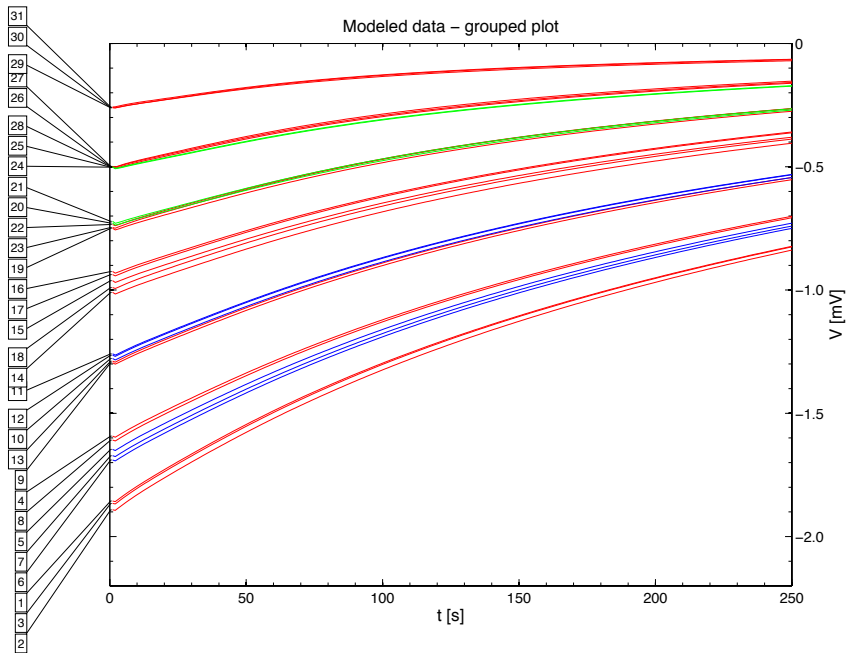


Figure 4.15: The modeled data in the first 250 s and grouped by location. The colors represent the location of the corresponding electrode. Green, red and blue represent the fine, medium and coarse sand in the model respectively. Compare with the measured data in Figure 4.14.

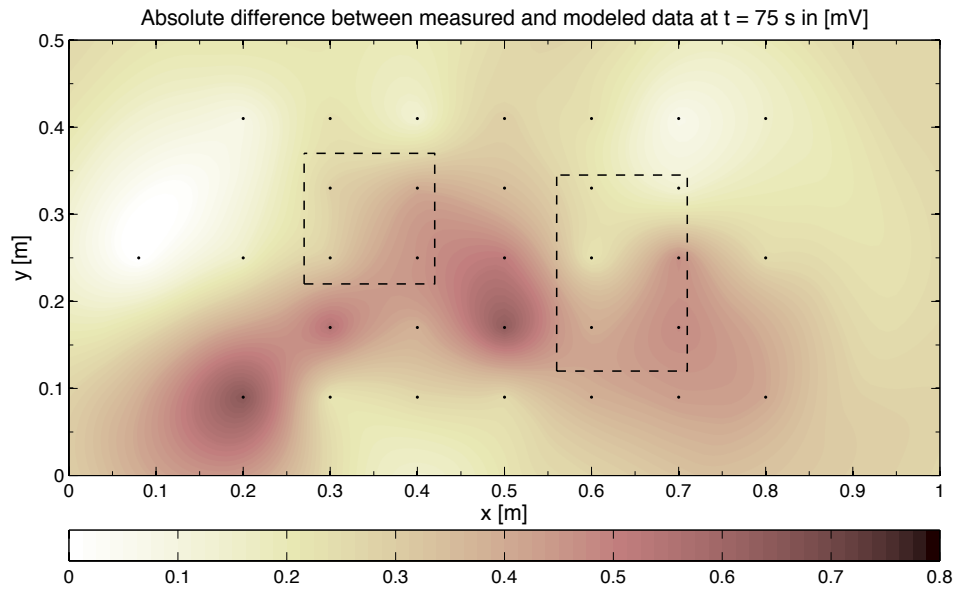


Figure 4.16: A contour plot of the absolute difference between the modeled data and the measured data at  $t = 75$  s. The colours represent the difference in surface potential in [mV], where the darker colors are bigger differences and the lighter colors differences towards 0. The small dots represent the Ag-AgCl electrodes. This contour was plotted using Matlab's Kriging Toolbox. The Semivariance for this operation can be found in Figure 4.17.

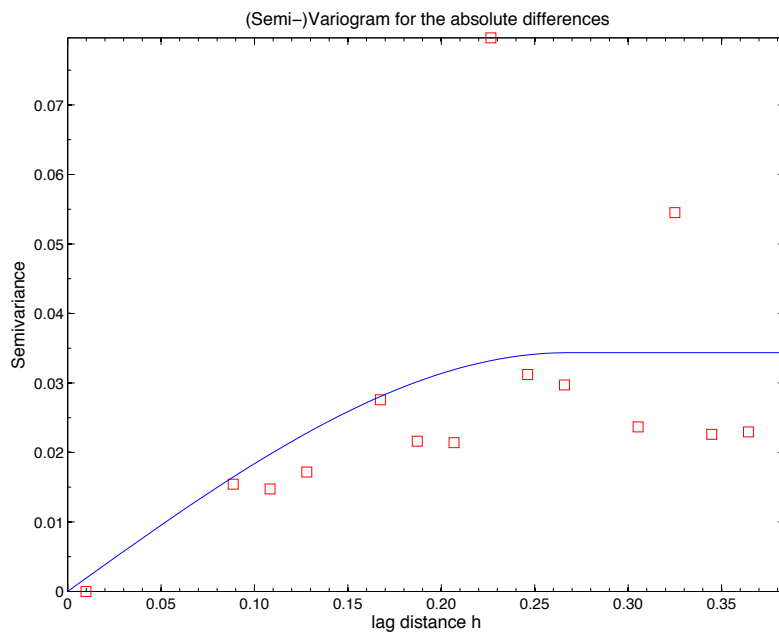


Figure 4.17: The semi-variance for the absolute difference between the measured and modeled data. The red dots show the semi-variance values, where the blue line is the fit that was used for the Kriging to construct Figure 4.16. This figure shows a good fit.

These differences were quantified by calculating the correlation coefficient for a linear fit. This was done with the Matlab *corr* function, using the 'Pearson' option, and was plotted in Figure 4.18. This coefficient has no unit. The closer the correlation coefficient is to 1, the higher the linear correlation is between the two data sets. A correlation coefficient of 0 means no correlation, where a correlation of 1 means 100% correlation. To make Figure 4.18, the correlation coefficients were calculated over the full 800 s time window and for each channel separately. Subsequently, they were interpolated and extrapolated to fill the full contour. Theoretically, the linear correlation of the reference electrodes in both the measured and modeled data should be 1, because they are both the constant function zero. The Matlab *corr* function however returns a *NaN*, because it finds a division by zero. In Figure 4.18, the value for the correlation coefficient at the reference electrode location is forced to be 1.

The errors of all channels ranges from 0.9525 to 0.9995, showing that there is meaningful linear correlation between the measured and the modeled data for all channels. The overall average error over all electrodes (minus the reference electrode) amounts 0.9934.

Figure 4.19 shows the semivariogram for the contour map in Figure 4.18. The red dots represent the semivariance points. The blue line is the model that was used to fit the semivariance. The data is far apart from each other, so the fit is not perfect. This might cause the plot to be biased.

Especially channel 30 and 31 and to a lesser extend channel 29 negatively stand out with a lower linear correlation coefficient than the overall impression. Overall, there is a gradient in the correlation, with increasing numbers towards the reference electrode. This might suggest that the reference electrode placement in the model is not correct, since the nearness of the reference electrode is a big influencing factor that determines the overall value of the data, as was mentioned previously in this section. Changing the position of the reference electrode would have a larger effect on the electrodes closeby, compared to electrode locations that are further away from the reference electrode. This might decrease the overall error in the data.



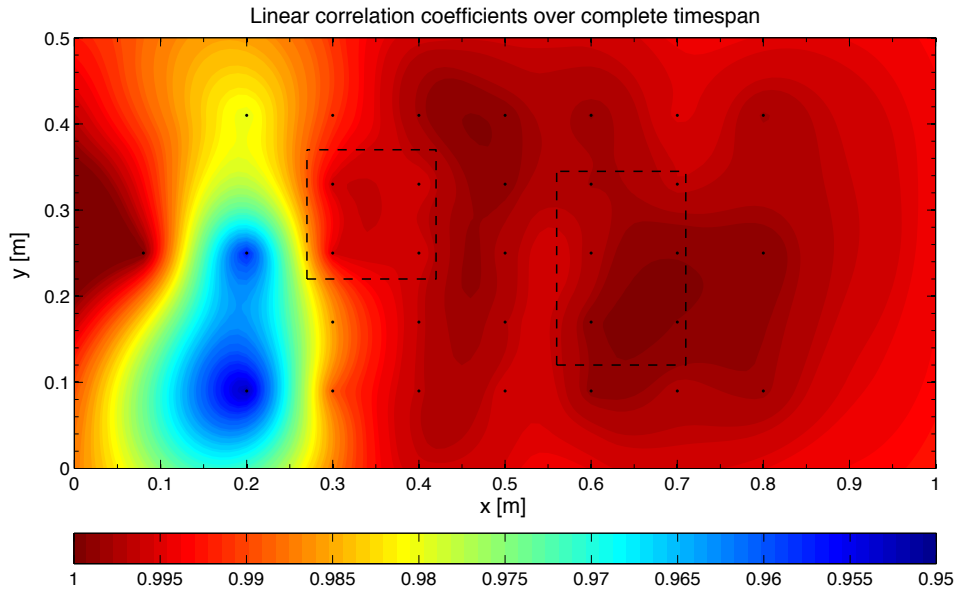


Figure 4.18: This contour plot of the Pearson linear correlation coefficient shows the local correlation coefficient between the modeled and the measured data for a linear fit. The correlation coefficient is a value between 0 and 1, where 1 means correlation (an exact match of the linear curve that fits the measured as well as the modeled data) and 0 means no correlation. This correlation coefficient was calculated for the full time span. The small dots represent the SP electrodes. The reference electrode is forced to 1. Figure 4.19 shows the semivariance and its fit used to produce this plot.

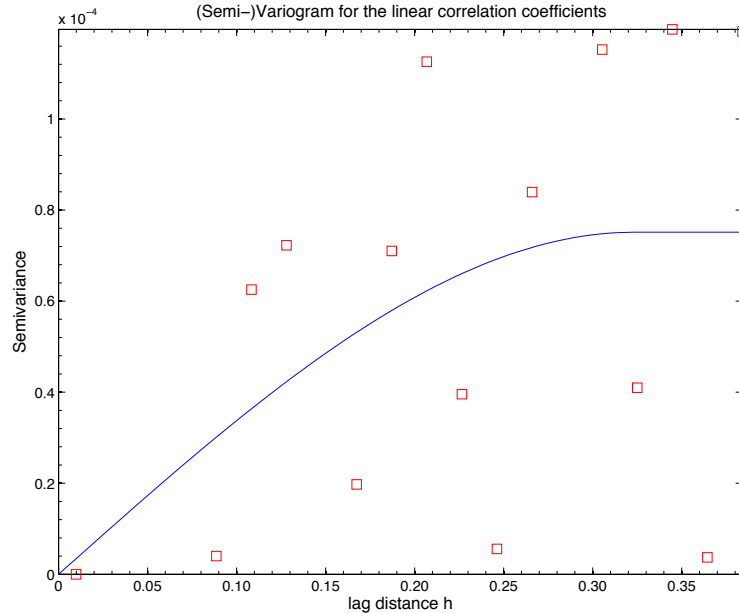


Figure 4.19: The semi-variance for the correlation coefficients. The red dots show the semi-variance values, where the blue line is the fit that was used for the Kriging to construct Figure 4.18.

## 4.5 Conclusions

Except for few channels (mainly 17 and 31, see Figure 4.6) that might have had some problems during the experiment and show deviant behaviour from the general trend in the data, the data have been successfully reproduced by a transient Comsol model. From the measured data, it is, to some extent possible to distinguish the different grain sizes below the subsurface of the tank. The Pearson linear correlation coefficients all lie within the 0.95 to 1.0 range, averaging at  $\pm 0.99$ . This indicates sufficient linear correlation between the measured and modeled data. And all this was done using reasonable values for solving the hydrological, solute transport and electrical models (refer to Table B.1). Even without inversion, one can already discriminate between areas with different hydraulic parameters. Inversion would only improve the location and correctness of the data.

---

# 5

## Stationary experiment: Direct Current Resistivity (DC Resistivity) & Induced Polarization (IP)

### 5.1 Introduction

This chapter discusses the measurements using the same setup as was used in Chapter 4 and as described in Chapter 3. However, the measurements from Chapter 4, produced under transient conditions, where the direct current resistivity and induced polarization experiments were taken under hydrologically steady-state conditions (a constant head gradient of zero between the two reservoirs). The DC resistivity method is mostly dependent of the electrical conductivity of the fluid, at least when the surface conductivity around the grains in the electrical double layer can be neglected. So, we do not expect to see differences in the data over both the sand cores, since the fluid's parameters do not change with time. From the induced polarization measurements, however, we expect to be able to recognize both the sand columns with different grain properties. This is because the IP method is more sensitive on the grain's surface electrical double layer properties, rather than the pore fluid alone. For a clear explanation of DC resistivity, please refer to [Archie \[1942\]](#); [Waxman and Smits \[1968\]](#).

In order to ensure sufficient coupling between the electrodes and the subsurface medium, the water level was raised to 9 cm below the sand's surface.

### 5.2 Methods

#### 5.2.1 Electrodes and their placement

A two-dimensional grid of eight by eight non-polarizing electrodes was installed on the surface of the tank. To have good coverage of the tank, the spacing in the  $x$ -direction was different from the spacing in the  $y$ -direction, 11 and 5 cm respectively. The margin with the long sides of the tank was 3 cm, the margin with the short sides (the silk screens)

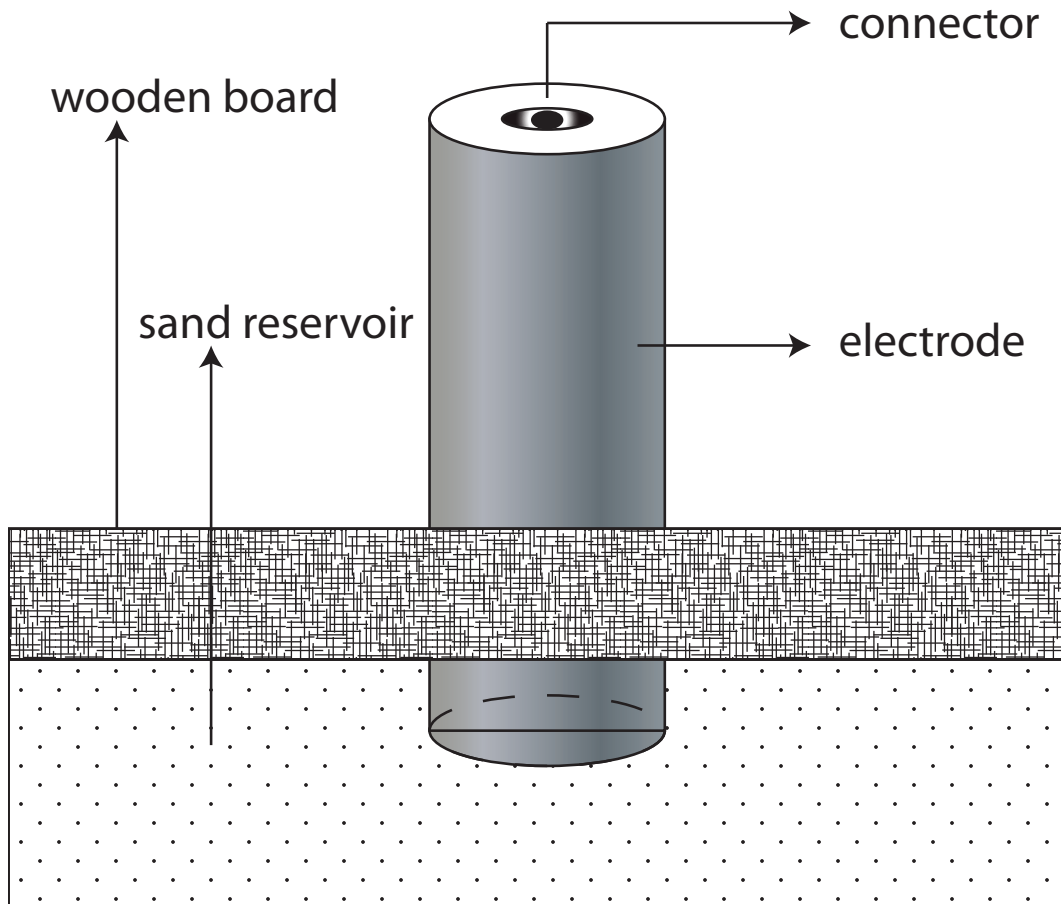


Figure 5.1: The electrodes were placed 2 cm into the sand aquifer and within a plywood sheet, in order to keep the electrodes in place while taking measurements.

was 6 cm. Figure 5.2 gives an overview of electrode placement for the DC resistivity and IP experiments. The numbers correspond to the numbers that were used in the ABEM protocol (see Section 5.2.2) file. For an explanation of the other elements of this figure, refer to Section 3.1.

To ensure sufficient electric coupling, the electrodes were inserted 2 cm into the sand cover. 64 Holes with the electrode diameter were drilled in a plywood board, such that the electrodes were held in place during the measurements. Refer to Figure 5.1 for a cross-section of one electrode placed in the plywood board. See Figure 5.5 and Figure 5.6 for the setup.

The electrodes are 30 mm in diameter by 125 mm in length and have an internal R of 400  $\Omega$ , where the static potential is  $\leq 0.1$  mV. They are highly stable non-polarizing electrodes and were designed for the purpose of these types of measurements. This information is from the supplier.<sup>1</sup>

<sup>1</sup>These electrodes are available from Geonesis in France ([www.geonesis.fr](http://www.geonesis.fr))

### 5.2.2 ABEM and protocol

DC resistivity and induced polarization measurements were conducted using the Terrameter SAS 4000 system<sup>2</sup>, which is depicted in Figure 5.3. When it measures IP, this system also measures DC resistivity. It was decided to try a more complicated setup of protocol file, that uses the full capability of the Terrameter, all 64 inputs and the 4 channels it can measure simultaneously. This way it is possible to measure pseudosections in two directions.

With help from the ABEM customer service<sup>3</sup>, a custom protocol was made for the reciprocal Schlumberger array (Figure 5.4). The protocol was designed to measure DC resistivity and IP values for all possible pseudosections in a 64 electrode setup. This resulted in 8 pseudosections in both directions, totalling 16 sections. Each of these sections consists of several measurements, where the reciprocal Schlumberger array was moved over the section of 8 electrodes. See Appendix C for the protocol file, the address file and some explanation about both. Because the ABEM apparatus is able to measure on four channels simultaneously, measuring the whole section only took between 30 minutes and one hour, depending on the settings for IP measurements (such as relaxation time, current injection time etc.). See Table 5.1 for the values that were used in the experiment that is discussed here.

Parameter	Value	Unit
Output	1	mA
Time on/off	0.5	s
Primary acquisition time	4	s
Initial delay	0.01	s
Base IP interval	0.02	s
Number of intervals	8	-

Table 5.1: Parameters used to set up the ABEM measurement routine.

---

<sup>2</sup>This system is available from the Sweden based ABEM ([www.abem.se](http://www.abem.se)).

<sup>3</sup>Many thanks to René Ruot for his input and time investment.

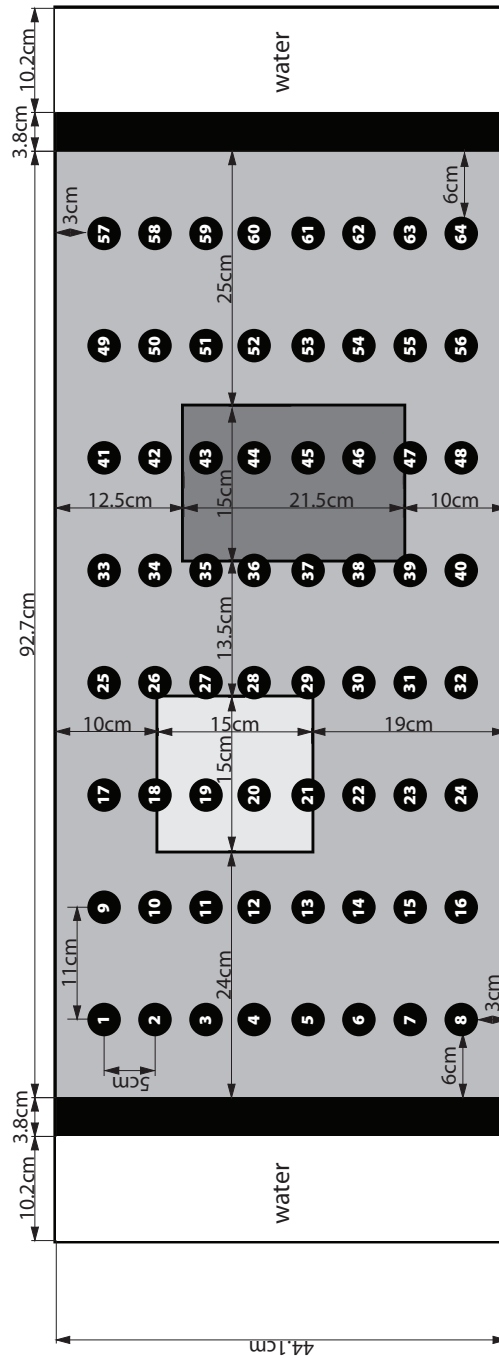


Figure 5.2: A schematic top view of electrode placement on the porous medium for the DC resistivity and IP measurements. The numbers correspond to the numbers that were defined in the ABEM protocol. The other elements are equivalent to those in Figure 3.1.



Figure 5.3: The ABEM Terrameter SAS 4000 system in action. The grey cable on the left is connected to a switcher box (also available from ABEM) which in also connected to two cables (visible in Figure 5.6) with 32 electrodes each.

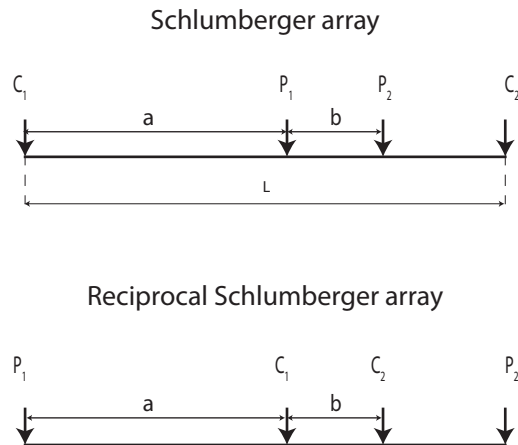


Figure 5.4: A schematic view of the regular (top) and the reciprocal (bottom) Schlumberger array.  $C1$  and  $C2$  indicate the current (injection) electrodes and the  $P1$  and  $P2$  the potential (measurement) electrodes. The distance  $L$  is the array length. Variables  $a$  and  $b$  decide the imaging depth of the array. Also refer to Figure 5.7.

### 5.2.3 Consequences of differing electrode spacing and array lengths

The different spacing between electrodes in the x- and y-direction results in a different imaging depth (Edwards [1977] and numerous others). According to Edwards [1977], a Schlumberger array, images at a depth of approximately  $1/5$  of the total length of the array (distance  $L$  in Figure 5.4). The array width depends on two things in this experiment: 1) the direction of the pseudosection (for an example of a pseudosection, see Figure 5.7, due to the different electrode spacings in the x- and y-direction and 2) the width of the actual array that was used to image one particular pseudopoint. In order to get more data points, different values for  $a$  and  $b$  (Figure 5.4) were used, resulting in pseudopoints at different depths. This is not a problem due to the design of the tank setup geometry: the heterogeneity only exists in the horizontal plane. Except for the small cover layer, the geometry is vertically symmetric. Additionally, the inversion software (RES3DINV) will take into account the different electrode spacings, by converting the pseudosections into real IP and DC resistivity sections.



Figure 5.5: The electrodes that were used for the DC resistivity and IP measurements were placed 2 cm into the sand aquifer and were kept in place by a plywood board.





Figure 5.6: The electrodes were connected to the ABEM switcher box by two customly designed cables, that have 32 electrode connectors each.

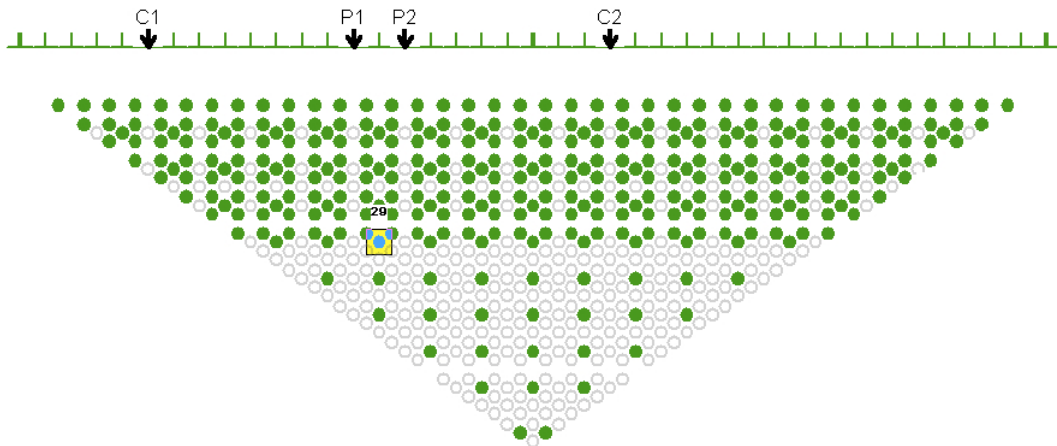


Figure 5.7: This figure shows an arbitrary pseudosection for a standard Schlumberger array. Every green dot represents a single measurement with a different array layout. For the blue dot, the array layout is mentioned on the surface.

## 5.3 Data

The fish tank that was used has insulating boundaries. These insulating boundaries introduce an error to the apparent resistance data. A code<sup>4</sup> was used in order to calculate the formation factor associated with such boundaries. After removing the formation factor, the data is ready for inversion and the inverted data should show no inference of the insulating boundaries.

To retrieve the real from the measured apparent DC resistivity and induced polarization values, inversion is needed. This inversion has been performed using RES3DINV<sup>5</sup>. This software iteratively inverts both the DC resistivity data as well as the IP data, using a least-squares algorithm. For inverting the IP data (see Section 2.5), the inverted DC resistivity data is needed, so for every iteration, it first solves for the DC resistivity problem and subsequently for the IP problem.

### 5.3.1 RES3DINV

RES3DINV is a software package that was developed to invert DC resistivity and induced polarization data, using a least-squares method. See Loke [2001]; Loke et al. [2006] for more technical and practical information about this software and inversion in general.

The output from RES3DINV was exported to Matlab, in order to be interpolated and extrapolated, in order to be plotted in horizontal cross-sectional contour maps over the full surface of the tank. Figure 5.8 shows the inverted DC resistivity data. RES3DINV reported an RMS error of 7.52 % for inverting the DC resistivity data. On the top and bottom edges, the real resistivity is different from the rest of the tank, even though the data has been corrected for the insulating boundaries. The left and right side are bounded by a water reservoir and then an insulating boundary. This water reservoir might have introduced an additional error, for which the data has not been corrected. The top and bottom effects might have been increased by the extrapolating that was used to fill the contour plot (in Figure 5.8). Furthermore, the coarse grained column, outlined with dashed lines in Figure 5.8 and on the right, has such larger grain size. There is sufficiently more pore fluid present that might have caused an increased conductivity and thus a lowered resistivity in that area. The total range of resistivity in the data is between approximately 30 and 60  $\Omega.m$ . This value is also close to the value that was used for the self-potential modeling in Section 4.4.

More interesting is the inverted IP data, which is shown in Figure 5.9. This image clearly shows an anomaly in the chargeability in the location where the coarse grained sand core lies in the subsurface. Both sand cores are outlined in dashed lines again and the chargeability is in the range of 1.07 - 1.08 [mV/V].

---

<sup>4</sup>Developed by Marios Karaoulis.

<sup>5</sup>Geotomo Software, Malaysia

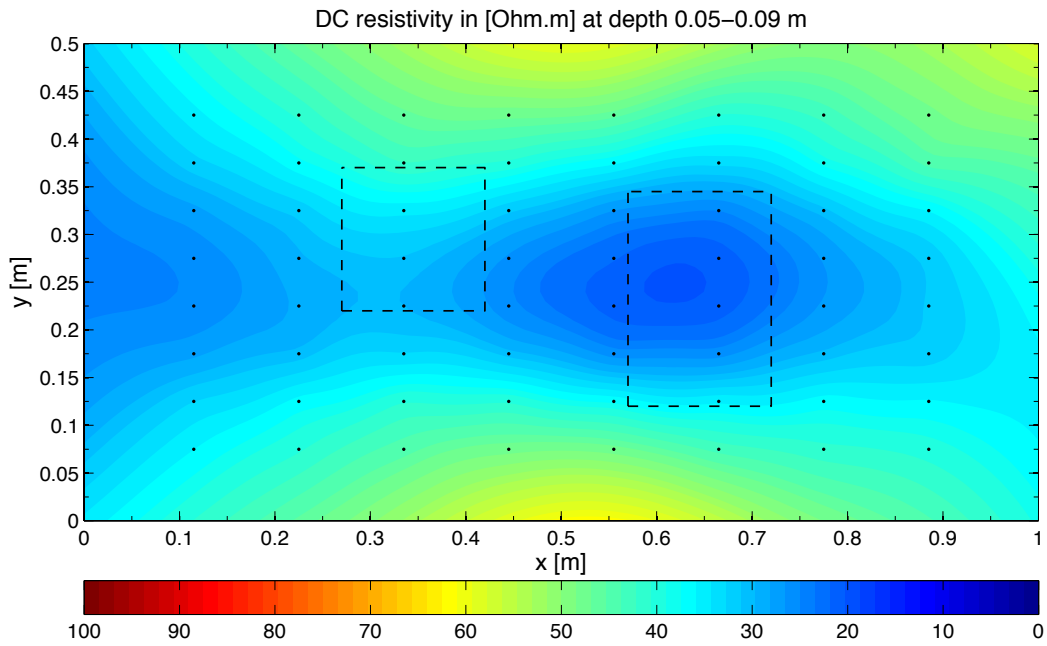


Figure 5.8: A contour plot of the inverted DC Resistivity data in  $\Omega.m$  and at depth 0.05-0.09 m. At this depth the sand cores are present. The small dots represent the locations of the electrodes, as mentioned in Figure 5.2. The inversion error, after three iterations was 7.52%.

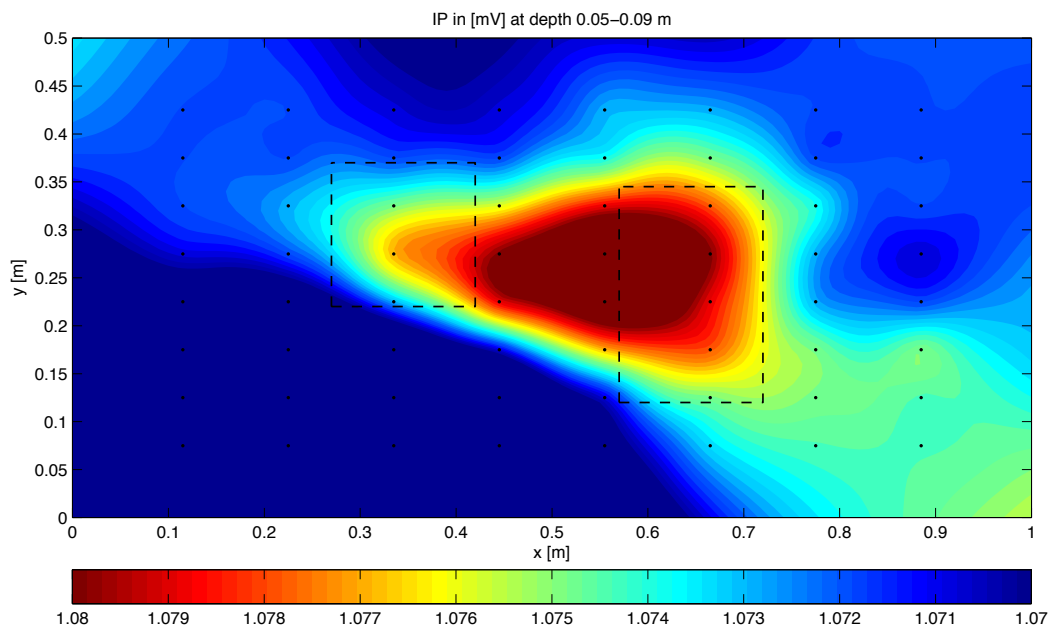


Figure 5.9: A contour plot of the inverted IP data in mV/V at depth 0.05-0.09. The small dots represent the locations of the electrodes, as mentioned in Figure 5.2. The inversion error, after three iterations was reported by RES3DINV to be 0.03 and the data ranges from 1.058 to 1.083.

## 5.4 Conclusions

As expected, from the DC resistivity data, not much can be said about the underlying geometry. The data have been corrected for insulating boundaries, but not for the water reservoir on either short side of the tank. This might have influenced the DC resistivity data, but the value differences are small (between 30 and 60  $\Omega.m$ ). Using the IP data, we were able to recognize an anomaly in chargeability at the location where the coarse grained sand column is situated. The anomaly is sufficiently large that, the rectangular column (with larger grain size) is recognizable, although the shape is distorted. Improvement of the DC resistivity image would also improve the IP image, since the DC resistivity is used in the IP inversion.

---

## 6

# Conclusions

The transient recovery experiment has shown that the self-potential method is able to show subsurface heterogeneities. The subsurface sand columns in the experiment are even outlined by the raw SP data. If this data would be inverted, the result would be improved.

A forward model for the transient SP recovery experiment was successfully built. The Pearson linear correlation coefficients between the modeled and measured data for the full 800s timespan, all lie within the 0.95 to 1.00 range and have an average of +/- 0.99. This is a decent number. The model can now be used in future inversion efforts.

The DC resistance data have been corrected for four insulating boundaries. The two short-side boundaries, however, have a water reservoir. Those might have influenced the DC resistivity data. An improvement can be made in those data. The resistivity has values between 30 and 60  $\Omega m$ , which are in the same order of magnitude as the resistivity used in the SP modeling. The SP signal that is measured is dependent on the resistivity distribution. So, improved resistivity distribution values will improve the (future) SP inversion and (present) IP inversion.

The IP data roughly shows the outlines of the coarse grained column and somewhat the finer grained column in the inverted data. The inversion of the IP data can probably be improved if the DC resistivity data is improved, since the DC resistivity data is used in the iterative inversion for the IP data.

Following this work, the SP data should be inverted. Using inversion codes for a combination of the SP and the DC resistivity and IP data sets should enable us to obtain higher quality information about permeability distributions in the aquifer.

## Appendix A

# Example values for several parameters

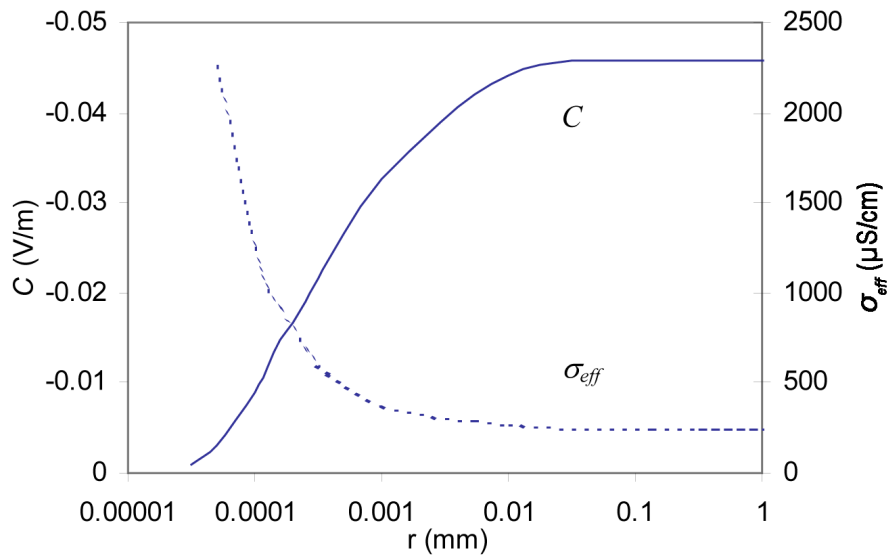
This appendix shows some example values for hydraulic conductivity, electrical conductivity and resistivity values for different rock types and different types of water as well as some information about the streaming potential coupling coefficient.

<b>Material</b>	<b>Hydraulic conductivity</b> $K[m/s]$
Gravel	$3 \times 10^{-4} - 3 \times 10^{-2}$
Coarse sand	$9 \times 10^{-7} - 6 \times 10^{-3}$
Medium sand	$9 \times 10^{-7} - 5 \times 10^{-4}$
Fine sand	$2 \times 10^{-7} - 2 \times 10^{-4}$
Silt, loess	$1 \times 10^{-9} - 2 \times 10^{-5}$
Glacial till	$1 \times 10^{-12} - 2 \times 10^{-6}$
Clay	$1 \times 10^{-11} - 5 \times 10^{-9}$
Unweathered marine clay	$8 \times 10^{-13} - 2 \times 10^{-9}$
Limestone, dolomite	$1 \times 10^{-9} - 6 \times 10^{-6}$
Sandstone	$3 \times 10^{-10} - 6 \times 10^{-6}$
Unfractured igneous and metamorphic rocks	$3 \times 10^{-14} - 2 \times 10^{-10}$

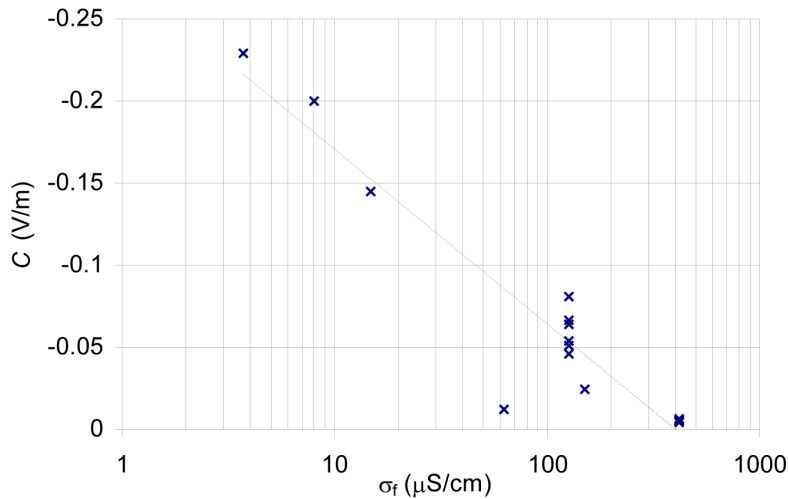
Table A.1: Typical hydraulic conductivity values for different rock types [Domenico and Schwartz, 1998]

<b>Fluid</b>	<b>Electrical conductivity</b> $\sigma_f[\mu S/cm]$
Groundwater (sediments)	$9 \times 10^{-7} - 6 \times 10^{-3}$
Distilled water	$9 \times 10^{-7} - 5 \times 10^{-4}$

Table A.2: Typical fluid conductivity values [Telford et al., 1990]



(a) Adapted from [Ishido and Mizutani \[1981\]](#), showing expected values from their capillary model.



(b) Image courtesy: [Sheffer \[2002\]](#). This figure was compiled with data from [Ishido and Mizutani \[1981\]](#); [Friborg \[1999\]](#); [Ogilvy et al. \[1969\]](#); [Ahmad \[1964\]](#).

*Figure A.1: (a) Shows the theoretical variation of the streaming potential coupling coefficient ( $C$ ) in the solid blue line and the effective conductivity ( $\sigma_{eff}$ ) in the dashed blue line, both with respect to the hydraulic radius and measured in a quartz-water system; (b) shows a logarithmic relation between the potential coupling coefficient ( $C$ ) and the fluid conductivity ( $\sigma_f$ ).*

Soil type	CEC [meq/100g]	Ion	Mobility [ $m^2/sV$ ]
Sand (1,7% organic, 7% clay)	6,3	$H^+$	$32.2 \times 10^{-8}$
		$OH^-$	$20.5 \times 10^{-8}$
Kaolinite	1-10	$SO_4^{2-}$	$8.3 \times 10^{-8}$
		$Na^+$	$5.2 \times 10^{-8}$
		$Cl^-$	$7.9 \times 10^{-8}$
		$K^+$	$7.6 \times 10^{-8}$
		$NO_3^-$	$7.4 \times 10^{-8}$
		$Li^+$	$4.0 \times 10^{-8}$
		$HCO_3^-$	$4.6 \times 10^{-8}$

(a) CEC values

(b) Ion mobility values

Table A.3: (a) gives typical values for the Cation Exchange Capacity (CEC), or the quantified capability of the grains in a porous medium to exchange cations, from McNeill [1980]; Keller and Frischknecht [1966]; Drever [1988]; (b) gives typical values for ionic mobility in solutions at 25°C [Keller and Frischknecht, 1966].



## Appendix B

# Modeling parameters

Hydrological and electrical parameters used for Comsol<sup>®</sup> modeling. No. 8, 30 and 70 correspond to the different sands that were used in the sandbox setup (coarse, medium and fine sand respectively). The column "variable name" gives the names for the parameters as they were used in the Comsol<sup>®</sup> model.

Parameter	Variable name	Value	Unit	Description
<b>General</b>				
<i>length</i>	x	1	m	Length as used in model
<i>width</i>	y	0.5	m	Width as used in model
<i>height</i>	z	0.4	m	Height (of the sand-filled part of the tank, as used in model)
$\rho_g$	rhog	2650	kg / m <sup>3</sup>	Grain density
$\rho_f$	rhof	998	kg / m <sup>3</sup>	Fluid density
<i>T</i>	T	23	°C	Temperature (measured)
$N_A$	N	$6.022 \times 10^{23}$	mol <sup>-1</sup>	Avogadro's constant
$k_B$	kB	$1.3806 \times 10^{-23}$	J/K	Boltzmann Constant (couples macro- and microscopic physics)
<b>Solute transport modeling</b>				
$\beta_+$	Bplus	$5 \times 10^{-8}$	m <sup>2</sup> /V s	Cation mobility
$\beta_-$	Bminus	$7 \times 10^{-8}$	m <sup>2</sup> /V s	Anion mobility
<b>Electrical modeling</b>				
<i>e</i>	e	$1.602 \times 10^{-19}$	C	Elementary charge
$\sigma_f$	sigmaF0	$2 \times 10^{-2}$	S / m	Fluid Conductivity (measured @ 23 °C)
$Q_v$ (08, 30 & 70)	Qv(08,30,70)	$10^{-9.2-0.82\log_{10}(k)}$	C/m <sup>-3</sup>	No. 08, 30 & 70 charge density (Empirical)

Parameter	Variable name	Value	Unit	Description
<b>Hydrological modeling</b>				
$H_{up}$	H_up	$H_0 + 0.045$	m	Higher head boundary condition definition
$H_{down}$	H_down	$H_0 - 0.045$	m	Lower head boundary condition definition
$H_0$	H0	0.13	m	Definition of height of boundary condition
$\eta_f$	nf	$1.002 \times 10^{-3}$	Pa s	Fluid viscosity
$D_{sand}$	Dsand	$1.5 \times 10^{-9}$	$m^2/s$	Molecular Diffusivity in Sand (thermal motion of particles)
$D_{res}$	Dres	$1 \times 10^{-6}$	$m^2/s$	Molecular Diffusivity in Reservoirs
$K$ (08)	K08	$1.5 \times 10^{-3}$	m/s	No. 8 Hydraulic conductivity
$K$ (30)	K30	$5 \times 10^{-4}$	m/s	No. 30 Hydraulic conductivity
$K$ (70)	K70	$5 \times 10^{-5}$	m/s	No. 70 Hydraulic conductivity
$\phi$ (8)	phi08	0.372	-	No. 8 Porosity
$\phi$ (30)	phi30	0.393	-	No. 30 Porosity
$\phi$ (70)	phi70	0.410	-	No. 70 Porosity
$d_{50}$ (8)	d08	$2 \times 10^{-2}$	cm	No. 8 grain size (50 <sup>th</sup> percentile)
$d_{50}$ (30)	d30	$5 \times 10^{-2}$	cm	No. 30 grain size (50 <sup>th</sup> percentile)
$d_{50}$ (70)	d70	$1.51 \times 10^{-1}$	cm	No. 70 grain size (50 <sup>th</sup> percentile)
$S_{wirr}$ (08)	Swirr08_vG	$6 \times 10^{-3}$	-	No. 8 Van Genuchten residual water saturation
$S_{wirr}$ (30)	Swirr30_vG	$3 \times 10^{-2}$	-	No. 30 Van Genuchten residual water saturation
$S_{wirr}$ (70)	Swirr70_vG	$5 \times 10^{-2}$	-	No. 70 Van Genuchten residual water saturation
$n_{vG}$ (08, 30 & 70)	n(08,30,70)_vG	1	-	No. 8, 30 & 70 Van Genuchten pore size distribution
$a_{vG}$ (08)	a08_vG	0.3154	1/cm	No. 8 Van Genuchten Inverse of Air Entry Suction
$a_{vG}$ (30)	a30_vG	$4.84 \times 10^{-2}$	1/cm	No. 30 Van Genuchten Inverse of Air Entry Suction
$a_{vG}$ (30)	a70_vG	$2.64 \times 10^{-2}$	1/cm	No. 70 Van Genuchten Inverse of Air Entry Suction
$\beta_s$	BetaS	$1 \times 10^{-7}$	$m^2/N$	Compressibility of solid
$\beta_l$	BetaL	$4.6 \times 10^{-10}$	$m^2/N$	Compressibility of fluid

Table B.1: Hydrological and electrical parameters used for Comsol<sup>®</sup> modeling. No. 8, 30 and 70 correspond to the different sands that were used in the sandbox setup (coarse, medium and fine sand respectively). The column "variable name" gives the names for the parameters as they were used in the Comsol<sup>®</sup> model. Some values were measured during or just before the experiment, others were taken from literature, such as see Sakaki and Itangasekare [2007]; Sakaki and Komatsu [2007]; Schroth et al. [1996]; Unimin Corporation [1997]

## Appendix C

# ABEM 3D protocol and address file

### C.1 Protocol file

Below the contents of the ABEM protocol file that was used to carry out the DC resistivity and IP measurements. The numbers represent the locations as mentioned in Figure 5.2. A 0 means no entry. If more than 4 electrodes are chosen, this means that there is more than one measurement (or array setup) in one line of text in the protocol-file. Every 5 lines below correspond to 9 measurements, totaling 144 measurements of pseudopoints, divided over 16 (8 in both the x- and y-direction) pseudosections.

```
0 Reciprocal-Schlumberger
8X8 Reciprocal-Schlumberger for 3D In-Line and Cross-Line measurements
2 3 1 4 0 0 0 0 0 0
3 4 2 5 1 6 0 0 0 0
4 5 3 6 2 7 1 8 0 0
5 6 4 7 3 8 0 0 0 0
6 7 5 8 0 0 0 0 0 0
10 11 9 12 0 0 0 0 0 0
11 12 10 13 9 14 0 0 0 0
12 13 11 14 10 15 9 16 0 0
13 14 12 15 11 16 0 0 0 0
14 15 13 16 0 0 0 0 0 0
18 19 17 20 0 0 0 0 0 0
19 20 18 21 17 22 0 0 0 0
20 21 19 22 18 23 17 24 0 0
21 22 20 23 19 24 0 0 0 0
22 23 21 24 0 0 0 0 0 0
26 27 25 28 0 0 0 0 0 0
27 28 26 29 25 30 0 0 0 0
28 29 27 30 26 31 25 32 0 0
29 30 28 31 27 32 0 0 0 0
30 31 29 32 0 0 0 0 0 0
34 35 33 36 0 0 0 0 0 0
```

35 36 34 37 33 38 0 0 0 0  
36 37 35 38 34 39 33 40 0 0  
37 38 36 39 35 40 0 0 0 0  
38 39 37 40 0 0 0 0 0 0  
42 43 41 44 0 0 0 0 0 0  
43 44 42 45 41 46 0 0 0 0  
44 45 43 46 42 47 41 48 0 0  
45 46 44 47 43 48 0 0 0 0  
46 47 45 48 0 0 0 0 0 0  
50 51 49 52 0 0 0 0 0 0  
51 52 50 53 49 54 0 0 0 0  
52 53 51 54 50 55 49 56 0 0  
53 54 52 55 51 56 0 0 0 0  
54 55 53 56 0 0 0 0 0 0  
58 59 57 60 0 0 0 0 0 0  
59 60 58 61 57 62 0 0 0 0  
60 61 59 62 58 63 57 64 0 0  
61 62 60 63 59 64 0 0 0 0  
62 63 61 64 0 0 0 0 0 0  
9 17 1 25 0 0 0 0 0 0  
17 25 9 33 1 41 0 0 0 0  
25 33 17 41 9 49 1 57 0 0  
33 41 25 49 17 57 0 0 0 0  
41 49 33 57 0 0 0 0 0 0  
10 18 2 26 0 0 0 0 0 0  
18 26 10 34 2 42 0 0 0 0  
26 34 18 42 10 50 2 58 0 0  
34 42 26 50 18 58 0 0 0 0  
42 50 34 58 0 0 0 0 0 0  
11 19 3 27 0 0 0 0 0 0  
19 27 11 35 3 43 0 0 0 0  
27 35 19 43 11 51 3 59 0 0  
35 43 27 51 19 59 0 0 0 0  
43 51 35 59 0 0 0 0 0 0  
12 20 4 28 0 0 0 0 0 0  
20 28 12 36 4 44 0 0 0 0  
28 36 20 44 12 52 4 60 0 0  
36 44 28 52 20 60 0 0 0 0  
44 52 36 60 0 0 0 0 0 0  
13 21 5 29 0 0 0 0 0 0  
21 29 13 37 5 45 0 0 0 0  
29 37 21 45 13 53 5 61 0 0  
37 45 29 53 21 61 0 0 0 0  
45 53 37 61 0 0 0 0 0 0  
14 22 6 30 0 0 0 0 0 0  
22 30 14 38 6 46 0 0 0 0  
30 38 22 46 14 54 6 62 0 0  
38 46 30 54 22 62 0 0 0 0  
46 54 38 62 0 0 0 0 0 0

```
15 23 7 31 0 0 0 0 0 0
23 31 15 39 7 47 0 0 0 0
31 39 23 47 15 55 7 63 0 0
39 47 31 55 23 63 0 0 0 0
47 55 39 63 0 0 0 0 0 0
16 24 8 32 0 0 0 0 0 0
24 32 16 40 8 48 0 0 0 0
32 40 24 48 16 56 8 64 0 0
40 48 32 56 24 64 0 0 0 0
48 56 40 64 0 0 0 0 0 0
```

## C.2 Address file

The address file, which is called in the protocol file above. This address file tells the ABEM machine which electrode is supposed to be used in each row of the protocol file. Depending on the layout of the cables connected to the ABEM, this file looks different. After a three line header, each row represents one electrode. The first number is the number that ABEM refers to when calling electrodes, the second number is the number with which the setup was built (and refers to the number as in Figure 5.2) and the last number combination is *cable – outtake*, so the number of the cable and the connector number on that particular cable.

```
8 8
1 0 1
64 8
1 32 1-1
2 31 1-2
3 30 1-3
4 29 1-4
5 28 1-5
6 27 1-6
7 26 1-7
8 25 1-8
9 17 2-1
10 18 2-2
11 19 2-3
12 20 2-4
13 21 2-5
14 22 2-6
15 23 2-7
16 24 2-8
17 16 3-1
18 15 3-2
19 14 3-3
20 13 3-4
21 12 3-5
22 11 3-6
23 10 3-7
24 9 3-8
```

25 1 4-1  
26 2 4-2  
27 3 4-3  
28 4 4-4  
29 5 4-5  
30 6 4-6  
31 7 4-7  
32 8 4-8  
33 33 5-1  
34 34 5-2  
35 35 5-3  
36 36 5-4  
37 37 5-5  
38 38 5-6  
39 39 5-7  
40 40 5-8  
41 48 6-1  
42 47 6-2  
43 46 6-3  
44 45 6-4  
45 44 6-5  
46 43 6-6  
47 42 6-7  
48 41 6-8  
49 49 7-1  
50 50 7-2  
51 51 7-3  
52 52 7-4  
53 53 7-5  
54 54 7-6  
55 55 7-7  
56 56 7-8  
57 64 8-1  
58 63 8-2  
59 62 8-3  
60 61 8-4  
61 60 8-5  
62 59 8-6  
63 58 8-7  
64 57 8-8

# Bibliography

- M.U. Ahmad. A laboratory study of streaming potentials. *Geophysical Prospecting*, 12(1):49–64, 1964. ISSN 1365-2478. doi: 10.1111/j.1365-2478.1964.tb01889.x. URL <http://dx.doi.org/10.1111/j.1365-2478.1964.tb01889.x>.
- G.E. Archie. The electrical resistivity log as an aid in determining some reservoir characteristics. *Petroleum Transactions of AIME*, 146:54–62, 1942.
- G.E. Archie. Electrical resistivity an aid in core-analysis interpretation. *American Association of Petroleum Geologists Bulletin*, 31(2):350–366, 1947.
- G.E. Archie. Introduction to petrophysics of reservoir rocks. *American Association of Petroleum Geologists Bulletin*, 34(5):943–961, 1950.
- G.E. Archie. Classification of carbonate reservoir rocks and petrophysical considerations. *American Association of Petroleum Geologists Bulletin*, 36(2):278–298, 1952.
- E. Aristodemou and A. Thomas-Betts. Dc resistivity and induced polarisation investigations at a waste disposal site and its environments. *Journal of Applied Geophysics*, 44(2-3):275–302, 2000.
- T. Arora, N. Linde, A. Revil, and J. Castermant. Non-intrusive characterization of the redox potential of landfill leachate plumes from self-potential data. *Journal of contaminant hydrology*, 92(3-4):274–292, 2007.
- H.C. Barlebo, M.C. Hill, and D. Rosbjerg. Investigating the macrodispersion experiment (made) site in columbus, mississippi, using a three-dimensional inverse flow and transport model. *Water Resources Research*, 40(4):W04211, 2004. ISSN 0043-1397.
- A. Binley and W. Daily. The performance of electrical methods for assessing the integrity of geomembrane liners in landfill caps and waste storage ponds. *Journal of Environmental and Engineering Geophysics*, 8:227, 2003.
- A. Boleve. *Localisation et quantification des zones de fuites dans les digues et les barrages par la méthode du potentiel spontané*. PhD thesis, Université de Savoie, March 2009.
- A. Boleve, A. Revil, C. Gevaudan, F. Janod, JL Mattiuzzo, and JJ Fry. Preferential fluid flow pathways in embankment dams imaged by self-potential tomography, near surf, 2009.
- G. Buselli and K. Lu. Groundwater contamination monitoring with multichannel electrical and electromagnetic methods. *Journal of Applied Geophysics*, 48(1):11–23, 2001.



- J. Castermant, CA Mendonça, A. Revil, F. Trolard, G. Bourrié, and N. Linde. Redox potential distribution inferred from self-potential measurements associated with the corrosion of a burden metallic body. *Geophysical Prospecting*, 56(2):269–282, 2008.
- S. Constable and L.J. Srnka. An introduction to marine controlled-source electromagnetic methods for hydrocarbon exploration. *Geophysics*, 72(2):WA3–WA12, March–April 2007.
- A. Crespy, A. Revil, N. Linde, S. Byrdina, A. Jardani, A. Bolève, and P. Henry. Detection and localization of hydromechanical disturbances in a sandbox using the self-potential method. *Journal of Geophysical Research*, 113(B1):B01205, 2008. ISSN 0148-0227.
- H. Darcy. *Les fontaines publiques de la ville de Dijon*. V. Dalmont, Libraire des Corps impériaux des ponts et chaussées et des mines, 1856.
- P.A. Domenico and F.W. Schwartz. *Physical and chemical hydrogeology*. Wiley New York, 1998. ISBN 0471597627.
- J.I. Drever. *The geochemistry of natural waters*. Prentice Hall, Englewood Cliffs, New Jersey, 1988.
- L.S. Edwards. A modified pseudosection for resistivity and ip. *Geophysics*, 42:1020, 1977.
- J. Friberg. Experimental and theoretical investigations into the streaming potential phenomenon with special reference to applications in glaciated terrain. 1999. ISSN 1402-1544.
- P.W.J. Glover. A generalized archie’s law for n phases. *Geophysics*, 75(6):E247, 2010.
- A. Haas and A. Revil. Electrical burst signature of pore-scale displacements. *Water Resources Research*, 45(10):W10202, 2009.
- R. Herman. An introduction to electrical resistivity in geophysics. *American Journal of Physics*, 69:943, 2001.
- T. Ishido and H. Mizutani. Experimental and theoretical basis of electrokinetic phenomena in rock-water systems and its applications to geophysics. *Journal of Geophysical Research*, 86(B3):1763–1775, 1981. ISSN 0148-0227.
- A. Jardani, A. Revil, F. Akoa, M. Schmutz, N. Florsch, and JP Dupont. Least squares inversion of self-potential (sp) data and application to the shallow flow of ground water in sinkholes. *Geophysical Research Letters*, 33(19):L19306, 2006. ISSN 0094-8276.
- A. Jardani, A. Revil, A. Boleve, A. Crespy, JP Dupont, W. Barrash, and B. Malama. Tomography of the darcy velocity from self-potential measurements. *Geophys. Res. Lett.*, 34, 2007.
- G.V. Keller and F.C. Frischknecht. Electrical methods in geophysical prospecting. international series of monographs in electromagnetic waves, vol. 10, 1966.
- R. Kirsch. *Groundwater geophysics: a tool for hydrogeology*. Springer, 2006.
- Y. Li and D.W. Oldenburg. 3-d inversion of induced polarization data. *Geophysics*, 65(6):1931–1945, 2000.
- M.H. Loke. Tutorial: 2-d and 3-d electrical imaging surveys. *Geotomo Software, Malaysia*, 2001.

- M.H. Loke, J.E. Chambers, and R.D. Ogilvy. Inversion of 2d spectral induced polarization imaging data. *Geophysical Prospecting*, 54(3):287–301, 2006.
- A. Mainault, Y. Bernabé, and P. Ackerer. Detection of advected concentration and ph fronts from self-potential measurements. *Journal of Geophysical Research*, 110(B11):B11205, 2005. ISSN 0148-0227.
- A. Mainault, Y. Bernabé, and P. Ackerer. Detection of advected, reacting redox fronts from self-potential measurements. *Journal of contaminant hydrology*, 86(1-2):32–52, 2006. ISSN 0169-7722.
- L. Marescot, R. Monnet, and D. Chapellier. Resistivity and induced polarization surveys for slope instability studies in the swiss alps. *Engineering Geology*, 98(1-2):18–28, 2008.
- J.D. McNeill. *Electrical conductivity of soils and rocks*. Geonics Limited, 1980.
- C.A. Mendonça. Forward and inverse self-potential modeling in mineral exploration. *Geophysics*, 73(1):F33–F43, January-February 2008.
- B.J. Minsley, J. Sogade, and F.D. Morgan. Three-dimensional source inversion of self-potential data. *J. Geophys. Res*, 112, 2007a.
- B.J. Minsley, J. Sogade, and F.D. Morgan. Three-dimensional self-potential inversion for subsurface dnapl contaminant detection at the savannah river site, south carolina. *Water Resour. Res*, 43, 2007b.
- J.K. Mitchell. Conduction phenomena: from theory to geotechnical practice. *Geotechnique*, 41(3):299–340, 1991. ISSN 0016-8505.
- J. Moore, A. Boleve, J. Sanders, and S. Glaser. Geophysical investigation of moraine dam seepage. In *Geophysical Research Abstracts*, volume 12. EGU, 2010.
- A.A. Ogilvy, M.A. Ayed, and V.A. Bogoslovsky. Geophysical studies of water leakages from reservoirs. *Geophysical Prospecting*, 17(1):36–62, 1969. ISSN 1365-2478.
- T.V. Panthulu, C. Krishnaiah, and J.M. Shirke. Detection of seepage paths in earth dams using self-potential and electrical resistivity methods. *Engineering Geology*, 59(3-4):281–295, 2001.
- D.S. Parasnis. *Principles of applied geophysics*. CRC Press, 1997.
- D. Patella and D. Schiavone. Comparative analysis of time domain and frequency domain in the induced polarization prospecting method. *Geophysical Prospecting*, 25(3):496–511, 1977.
- A. Revil and N. Florsch. Determination of permeability from spectral induced polarization in granular media. *Geophysical Journal International*, 2010.
- A. Revil and P. Leroy. Governing equations for ionic transport in porous shales. *J. Geophys. Res*, 109, 2004.
- A. Revil, F. Trolard, G. Bourrié, J. Castermant, A. Jardani, and CA Mendonça. Ionic contribution to the self-potential signals associated with a redox front. *Journal of contaminant hydrology*, 2009.

- A. Rozycki. Evaluation of the streaming potential effect of piping phenomena using a finite cylinder model. *Engineering Geology*, 104(1-2):98–108, 2009. ISSN 0013-7952.
- A. Rozycki, J.M. Ruiz Fonticiella, and A. Cuadra. Detection and evaluation of horizontal fractures in earth dams using the self-potential method. *Engineering Geology*, 82(3):145–153, 2006. ISSN 0013-7952.
- Y. Rubin and S.S. Hubbard. *Hydrogeophysics*, volume 59. Springer Verlag, 2005.
- KR Rushton. *Groundwater hydrology: Conceptual and computational models*. John Wiley & Sons Inc, 2003.
- T. Sakaki and T.H. Illangasekare. Comparison of height-averaged and point-measured capillary pressure–saturation relations for sands using a modified tempe cell. *Water Resources Research*, 43(12):W12502, 2007.
- T. Sakaki and M. Komatsu. Physical and hydraulic properties of silica sands for laboratory experiments. unpublished technical notes, 08 2007.
- C. Schlumberger. Method and apparatus for identify, 1939. US Patent 2,165,013.
- M.H. Schroth, S.J. Ahearn, J.S. Selker, and J.D. Istok. Characterization of miller-similar silica sands for laboratory hydrologic studies. *Soil Science Society of America Journal*, 60(5):1331–1339, 1996.
- M.R. Sheffer. Response of the self-potential method to changing seepage conditions in embankment dams. Master’s thesis, UNIVERSITY OF BRITISH COLUMBIA, 2002.
- W.R. Sill. Self-potential modeling from primary flows. *Geophysics*, 48(1):76–86, January 1983.
- RW Sillars. The properties of a dielectric containing semiconducting particles of various shapes. *Wireless Section, Institution of Electrical Engineers-Proceedings of the*, 12(35):139–155, 1937.
- L. Slater. Near surface electrical characterization of hydraulic conductivity: from petrophysical properties to aquifer geometries—a review. *Surveys in Geophysics*, 28(2):169–197, 2007.
- O. Stern. The theory of the electrolytic double-layer. *Z. Elektrochem*, 30:508–516, 1924.
- B. Suski, E. Rizzo, and A. Revil. A sandbox experiment of self-potential signals associated with a pumping test. *Vadose Zone Journal*, 3(4):1193, 2004.
- W.M. Telford, W.M. Telford, LP Geldart, and R.E. Sheriff. *Applied geophysics*. Cambridge Univ Pr, 1990. ISBN 0521339383.
- K. Titov, V. Komarov, V. Tarasov, and A. Levitski. Theoretical and experimental study of time domain-induced polarization in water-saturated sands. *Journal of Applied Geophysics*, 50(4):417–433, 2002.
- P. Tsourlos and R. Ogilvy. An algorithm for the 3-d inversion of tomographic resistivity and induced polarisation data: preliminary results. *Journal of the Balkan Geophysical Society*, 2(2):30–45, 1999.

- Unimin Corporation. Granusil mineral fillers, technical data, 2 pp. Technical report, Emmett, Idaho., 1997.
- H.L.F. von Helmholtz. Some laws concerning the distribution of electrical currents in conductors. *Ann. Physik*, 89:211, 1853.
- Karl Willy Wagner. Erklärung der dielektrischen nachwirkungsvorgänge auf grund maxwellscher vorstellungen. *Electrical Engineering (Archiv fur Elektrotechnik)*, 2(9):371–387, 1914. doi: 10.1007/BF01657322.
- S.H. Ward and W.R. Sill. Resistivity, induced polarization, and self-potential methods in geothermal exploration. Master's thesis, 1982.
- MH Waxman and LJM Smits. A electrical conductivities in oil-bearing shaly sands, 1968.
- D.D. Wheaton. Investigating the impact of advective and diffusive controls in solute transport on geoelectrical data. Master's thesis, The Pennsylvania State University, 2009.
- D.D. Wheaton and K. Singha. Investigating the impact of advective and diffusive controls in solute transport on geoelectrical data. *Journal of Applied Geophysics*, 72(1):10–19, 2010.

# List of Figures

1.1	A flowchart, taken from Slater [2007], summarizing efforts to characterize aquifer geometries using geoelectrical measurements. . . . .	5
2.1	(a) schematic representation of the pore space between two grains in a porous medium.; (b) schematic view of conduction and convection vectors under flow in a porous medium; (c) A sketch showing the Stern and the diffuse layers. It also shows the distribution of ionic species in the pore space at equilibrium. $Q_v$ is the volumetric charge density (in $Cm^3$ and corresponds to the charge of the diffuse layer). . . . .	11
2.2	The IP decay curve. The chargeability is measured as the area between two time values. For example $M_{20,40}$ represents the chargeability measured in the interval between 20-40 msec. The delay before the measurements starts are denoted by $t_D = t_1$ . This figure was taken from the ABEM SAS 1000 / 4000 manual document. . . . .	15
3.1	Schematic figure showing the sand box setup as used for the SP experiment. The upper figure is a top view, the lower a side view, along the long side and through the middle of the tank. Note the different grain sizes and the head difference between the two water reservoirs. The numbers represent sensor locations for the SP experiment. The dashed line through the middle is where the cross section (below) was taken. This figure is to scale. . . . .	18
3.2	A view of how the sand columns were constructed, using metal shields to prevent the sides to collapse in unstable saturated sand. . . . .	19
3.3	Upon completion, this is what the sand columns look like. Top view. The black bar in the middle is part of the plastic reinforcement that runs along the edges of the tank and is meant to increase its structural integrity. . . . .	19
4.1	(a) A schematic view of the transient SP experiment, as described in Section Chapter 4. The peristaltic pump pumps water from the left reservoir to the water reservoir on the right, creating a hydraulic head difference between both ends. (b) An example of a peristaltic pump. This is not the actual pump that was used in these experiments. Image courtesy: Eijkelkamp Agrisearch Equipment ( <a href="http://www.eijkelkamp.com">www.eijkelkamp.com</a> ). . . . .	23

4.2	Top view of the experimental tanks, just after installing the non-polarizing Ag-Cl electrodes and just before covering them up with a small layer of sand. These electrodes were placed just below the surface to ensure good electrical coupling with the porous medium. Sensors 14-18 are not visible due to the reinforcement bar of the tank. The inset is an example of two Biosemi Ag-AgCl, amplified, non-polarizing electrodes. . . . .	24
4.3	Raw data that came from the SP experiments. Here channel 10 is shown as an example. Channel 10 shows a typical electrical response that was measured in both SP experiments. The y-axis shows the measured potential of the channel in microvolts, referenced to the reference electrode. The blue data is the raw data from the Biosemi <sup>®</sup> , divided by the gain of 32, and the red line is after resampling the raw data. The green vertical line indicates the beginning of the experiment, the moment when the peristaltic pump is shut off. . . . .	26
4.4	The same data as in Figure 4.3, but here, the red curve represents the 2 <sup>nd</sup> order polynomial that was fit to the data and will be used to detrend the data, in order to remove low frequency noise. . . . .	27
4.5	Detrended data for channel 10. The red line represents the 2 <sup>nd</sup> order polynomial that had been detracted from the data. This is zero, since it has been detracted from itself. The solid blue line is the detrended data in mV. . . . .	27
4.6	The measured data over the first 800 seconds of elapsed time during the experiment. Every line represents the SP signal of a single channel, which are numbered on the left. . . . .	28
4.7	A contour plot of the measured data at $t = 75$ . The color bar shows the value of the surface electrical potential in mV. The effects of the two sand columns, outlined by a dashed line. The contouring was done, using Matlab and the Kriging Toolbox. Figure 4.8 shows the semivariance for the Kriging that was performed for this contour plot. . . . .	29
4.8	The semi-variance for the measured data. The red dots show the semi-variance values. The blue line shows the fit that was used for the Kriging to construct Figure 4.7. This fit is good enough to avoid biasing of the Kriging image. . . . .	29
4.9	Results of the initial subdomain model, that was used as the initial value for transient SP modeling. This model has boundary conditions as mentioned in Table B.1 (26.3 cm for $x = 0$ and 17.3 cm for $x = 1$ ). The three isosurfaces, dark blue, light blue and dark red, represent the 100, 75 and 50% saturation levels, the vertical cross-sections the pressure head [m] and the arrows correspond to the relative flow velocity and flow direction. . . . .	31
4.10	A snapshot of the transient model while it is solving. This snapshot was taken at $t=250$ s. One can see the water saturation at 100%, 75% and 50% levels in dark blue, light blue and dark red isosurfaces respectively. At closer inspection, it is visible that the water saturation levels have not reached equilibrium yet (where $x=0$ the 100% level is approximately 10% higher than at $x=1$ ). The arrows indicate flow direction and their size represent relative flow velocity. The contour slice at $z=0.4$ , with coloured scalebar to the right, represents the actual surface potential at $t=75$ s. See text for further explanation. . . . .	33
4.11	This plot shows the complete timespan for the modeled data. The numbers on the left represent the SP sensors (see to Figure 3.1 for exact locations). Compare with the measured data in Figure 4.6. . . . .	34

4.12	A contour plot of the modeled data at $t = 75$ . The color bar shows the value of the surface electrical potential in mV. The small dots represent the positions of the SP electrodes. . . . .	34
4.13	This figure shows the measured (in blue) as well as the modeled (in red) data for the complete modeled time window. Self-potential signals are in mV and time is in seconds. . . . .	36
4.14	This plot shows the first 250 seconds of the experiment, where every line represents the SP signal of a single channel, annotated on the left margin of the figure. . . . .	37
4.15	The modeled data in the first 250 s and grouped by location. The colors represent the location of the corresponding electrode. Green, red and blue represent the fine, medium and coarse sand in the model respectively. Compare with the measured data in Figure 4.14. . . . .	37
4.16	A contour plot of the absolute difference between the modeled data and the measured data at $t = 75$ s. The colours represent the difference in surface potential in [mV], where the darker colors are bigger differences and the lighter colors differences towards 0. The small dots represent the Ag-AgCl electrodes. This contour was plotted using Matlab's Kriging Toolbox. The Semivariance for this operation can be found in Figure 4.17. . . . .	38
4.17	The semi-variance for the absolute difference between the measured and modeled data. The red dots show the semi-variance values, where the blue line is the fit that was used for the Kriging to construct Figure 4.16. This figure shows a good fit. . . . .	38
4.18	This contour plot of the Pearson linear correlation coefficient shows the local correlation coefficient between the modeled and the measured data for a linear fit. The correlation coefficient is a value between 0 and 1, where 1 means correlation (an exact match of the linear curve that fits the measured as well as the modeled data) and 0 means no correlation. This correlation coefficient was calculated for the full time span. The small dots represent the SP electrodes. The reference electrode is forced to 1. Figure 4.19 shows the semivariance and it's fit used to produce this plot. . . . .	40
4.19	The semi-variance for the correlation coefficients. The red dots show the semi-variance values, where the blue line is the fit that was used for the Kriging to construct Figure 4.18. . . . .	40
5.1	The electrodes were placed 2 cm into the sand aquifer and within a plywood sheet, in order to keep the electrodes in place while taking measurements. . .	43
5.2	A schematic top view of electrode placement on the porous medium for the DC resistivity and IP measurements. The numbers correspond to the numbers that were defined in the ABEM protocol. The other elements are equivalent to those in Figure 3.1. . . . .	45
5.3	The ABEM Terrameter SAS 4000 system in action. The grey cable on the left is connected to a switcher box (also available from ABEM) which in also connected to two cables (visible in Figure 5.6) with 32 electrodes each. . . .	46
5.4	A schematic view of the regular (top) and the reciprocal (bottom) Schlumberger array. C1 and C2 indicate the current (injection) electrodes and the P1 and P2 the potential (measurement) electrodes. The distance L is the array length. Variables a and b decide the imaging depth of the array. Also refer to Figure 5.7. . . . .	46

5.5	The electrodes that were used for the DC resistivity and IP measurements were placed 2 cm into the sand aquifer and were kept in place by a plywood board. . . . .	47
5.6	The electrodes were connected to the ABEM switcher box by two customly designed cables, that have 32 electrode connectors each. . . . .	48
5.7	This figure shows an arbitrary pseudosection for a standard Schlumberger array. Every green dot represents a single measurement with a different array layout. For the blue dot, the array layout is mentioned on the surface. . . . .	48
5.8	A contour plot of the inverted DC Resistivity data in $\Omega.m$ and at depth 0.05-0.09 m. At this depth the sand cores are present. The small dots represent the locations of the electrodes, as mentioned in Figure 5.2. The inversion error, after three iterations was 7.52%. . . . .	50
5.9	A contour plot of the inverted IP data in mV/V at depth 0.05-0.09. The small dots represent the locations of the electrodes, as mentioned in Figure 5.2. The inversion error, after three iterations was reported by RES3DINV to be 0.03 and the data ranges from 1.058 to 1.083. . . . .	50
A.1	(a) Shows the theoretical variation of the streaming potential coupling coefficient ( $C$ ) in the solid blue line and the effective conductivity ( $\sigma_{eff}$ ) in the dashed blue line, both with respect to the hydraulic radius and measured in a quartz-water system; (b) shows a logarithmic relation between the potential coupling coefficient ( $C$ ) and the fluid conductivity ( $\sigma_f$ ). . . . .	54



# List of Tables

2.1	Primary and coupled flow phenomena (adapted from <a href="#">Mitchell [1991]</a> ). . . . .	7
4.1	Parameter values under which Experiment 1 and 2 respectively were performed.	22
5.1	Parameters used to set up the ABEM measurement routine. . . . .	44
A.1	Typical hydraulic conductivity values for different rock types [ <a href="#">Domenico and Schwartz, 1998</a> ] . . . . .	53
A.2	Typical fluid conductivity values [ <a href="#">Telford et al., 1990</a> ] . . . . .	53
A.3	(a) gives typical values for the Cation Exchange Capacity (CEC), or the quantified capability of the grains in a porous medium to exchange cations, from <a href="#">McNeill [1980]</a> ; <a href="#">Keller and Frischknecht [1966]</a> ; <a href="#">Drever [1988]</a> ; (b) gives typical values for ionic mobility in solutions at 25°C [ <a href="#">Keller and Frischknecht, 1966</a> ]. . . . .	55
B.1	Hydrological and electrical parameters used for Comsol <sup>®</sup> modeling. No. 8, 30 and 70 correspond to the different sands that were used in the sandbox setup (coarse, medium and fine sand respectively). The column "variable name" gives the names for the parameters as they were used in the Comsol <sup>®</sup> model. Some values were measured during or just before the experiment, others were taken from literature, such as see <a href="#">Sakaki and Illangasekare [2007]</a> ; <a href="#">Sakaki and Komatsu [2007]</a> ; <a href="#">Schroth et al. [1996]</a> ; <a href="#">Unimin Corporation [1997]</a>	58